ECTOPIC FIBROBLAST GROWTH FACTOR SIGNALING IN REPROGRAMMING PROSTATE CANCER CELL METABOLISM AND IMMUNE EVASION

A Dissertation

by

YUEPENG KE

Submitted to the Graduate and Professional School of
Texas A&M University
in partial fulfillment of the requirements for the degree of

DOCTOR OF PHILOSOPHY

Chair of Committee,	Fen Wang
Committee Members,	Clifford C Stephan
	Jianming Xu
	Yubin Zhou
Head of Department,	Amy Waer

May 2022

Major Subject: Medical Sciences

ABSTRACT

Prostate cancer (PCa) is the third leading cause of cancer death. The lack of an effective cure for advanced stages and an overall low response to immunotherapy give prominence to the critical need for developing novel therapies. PCa has an “immune cold” tumor microenvironment (TME), suggesting that immunotherapy can be enhanced by converting the immune “cold” TME to immune “hot” TME, which will be at the front lines to overcome immune evasion in PCa. Understanding the mechanism of PCa progression and TME remodeling will be essential to change the unfavorable TME and develop new therapeutic strategies.

To meet the challenges of bio-molecular synthesis for fast growth, cancer cells reprogram their metabolism to derive energy to aerobic glycolysis, and such reprograming usually results from a composite consequence of genetic and environmental changes. This includes the depletion of glucose and the accumulation of tumor-derived lactate. Together with the secretion of immunosuppressive cytokines, these contribute to establishing an immune “cold” TME, suggesting that suppression of metabolic reprogramming in cancer cells can be an effective way to inhibit immune evasion. However, as aerobic glycolysis and oxidative phosphorylation (OXPHOS) are also needed for T cell activation and function, general metabolic inhibitors directly targeting metabolism can disrupt hemostasis in T cells as well, and thus will not be effective for changing the immune “cold” tumors. A new cancer cell specific suppression of aerobic glycolysis without inhibiting T cell metabolism is needed to improve the PCa immunotherapy.

In this study, we report that deletion of ectopic FGFR1 signaling reduced aerobic glycolysis and promoted OXPHOS in PCa cells, suggesting a reversal of PCa metabolic reprogramming. Since normal T cells do not express FGFR1, it is expected that suppression of FGFR1 signaling can be a normal strategy to selectively target aerobic glycolysis in PCa cells to improve PCa immunotherapy. We found that conditioned medium from PCa cells suppressed T cell growth *in vitro*, potentially through tumor-derived cytokines and metabolites secreted. We observed blunting ectopic FGFR1 signaling either by inactivating *FGFR1* gene or by treating with FGFR tyrosine kinase inhibitor increased $CD3^+CD8^+$ T cells in the TRAMP PCa model, indicating that inactivating ectopic FGFR1 signaling facilitates penetration of T cells to the tumor. Moreover, this T-cell mediated immune response can be boosted by treating with anti-immune checkpoint antibody, anti-PD-1 antibody. In addition, bioinformatics analysis of the public database of the single-cell RNA sequence of human PCa revealed that the tumor with FGFR1 expression in epithelial cells was associated with a high $CD8\alpha^+$ T cell population, suggesting that high FGFR1 expression in epithelial cells suppressed infiltration of $CD8\alpha^+$ T cells, which is consistent with our data derived from PCa cell and mouse models.

Together, the data suggest that the combination of FGFR1 inhibitor and anti-checkpoint treatment can be an effective way to increase $CD8^+$ T cell-mediated immune response in prostate tumors, and therefore, reveals a novel strategy for PCa treatment.

DEDICATION

This work is dedicated to my beloved family, whose unconditional love, tireless support, and enthusiastic encouragement make possible fruition to our efforts.

ACKNOWLEDGEMENTS

I would like to express my appreciation and deepest gratitude to the following people who support me with their kindness, care, and encouragement during my graduate training and made this study possible.

I would like to thank my mentor, Dr. Fen Wang. He provided me the opportunity to join his lab and learn to conduct research. He is always nice, patient, and willing to give me guidance and the freedom to think independently, scientifically, and critically. What I have learned from him is a precious gem that will help my future life and career. He is a fantastic mentor who deserves respect and admiration.

I would like to thank my committee members, Dr. Yubin Zhou, Dr. Jianming Xu, and Dr. Clifford Stephan. My committee members gave me a lot of encouragement to handle the speech anxiety and inspired me in one way or another. Dr. Yubin Zhou gave me the chance to conduct part of the research in his lab after rotation and generously provide access to the optogenetic tools. His thoughtful comments and insightful advice are beneficial to my graduate training. Dr. Jianming Xu and Dr. Clifford Stephan posed incisive questions and valuable advice on the project. They generously shared the experience to keep the project on track, and their considerable expertise gave me the strength to carry on. Again, thank you all for your precious time, efforts, and support.

I would like to thank all our collaborators, Dr. Margie Moczygemba, Ms. Sevinj Iskenderova, Dr. Alex Walsh, Dr. Shu-Hsia Chen, and Dr. Yitian Xu, for their professional support and kind help. The collaboration between the labs added a broader perspective to this study.

I would like to extend my special thanks to Dr. Stefan Siwko, who helped me with the proofreading of my writings, and offered valuable advice and suggestions; to fabulous ladies Ms. Cynthia Lewis and Ms. Denelle Orellana, who helped me with all complicated paperwork and all other things that I could not handle by myself; to all m friends I met in Houston. Thank you all for your support.

Finally, I would like to thank my beloved family. To dad, mom, my husband, and all members of our big family: Thank you for your love, support, and encouragement. Thank you for always being there for me. Thank you for being such a vital part of my life journey. Thank you for everything.

CONTRIBUTORS AND FUNDING SOURCES

Contributors

This work was supervised by a dissertation committee consisting of Professors Fen Wang (advisor), Yubin Zhou, and Clifford Stephan from the Center for Translational Cancer Research in the Texas A&M University Institute of Biosciences and Technology, and Professor Jianming Xu from the Department of Molecular and Cellular Biology in Baylor College of Medicine.

The RNA-seq, single-cell RNA-seq, and IMC data analysis were conducted by Mr. Ziying Liu from the Center for Translational Cancer Research in Texas A&M Institute of Biosciences and Technology. The NAD(P)H / FAD fluorescence lifetime imaging was done by our collaborator Professor Alex J. Walsh, from the Department of Biomedical Engineering at Texas A&M University. The RT-PCR analysis and lactate production of purified mouse T cell experiments were performed by Dr. Junchen Liu from the Department of Integrative Biology and Pharmacology at The University of Texas Health Science Center at Houston. The Flow Cytometry data was acquired with the help of Professor Margie Moczygemba and Mrs. Sevinj Isgandarova from the Center for Infectious and Inflammatory Disease in the Texas A&M Institute of Biosciences and Technology. The IMC studies were done in collaboration with Professor Shu-Hsia Chen from the Center for Immunotherapy Research in Houston Methodist.

Funding Sources

This work was supported by the Cancer Prevention and Research Institutes of Texas (RP190612) to Dr. Fen Wang.

NOMENCLATURE

ADT	Androgen-deprivation therapy
ATP	Adenosine triphosphate
AR	Androgen receptor
BSA	Bovine serum albumin
CgA	Chromogranin A
CHKA	Choline kinase α
CM	Conditional medium
CPI	Immune checkpoint inhibitors
CPT1A	Carnitine palmitoyl-transferase 1A
CRPC	Castration-resistant prostate cancer
CRY2PHR	Photosensory protein cryptochrome 2
CTLA-4	Cytotoxic T-lymphocyte-associated protein 4
DEGs	Differentially expressed genes
DMEM	Dulbecco's modified eagle's medium
ECAR	Extracellular acidification rate
ETC	Electron transport chain
FACS	Fluorescence-activated cell sorting
$FADH_2$	Flavin adenine dinucleotide
FCCP	Carbonyl cyanide-4 (trifluoromethoxy) phenylhydrazone
FDA	Food and Drug Administration
FDG	^{18}F-fluorodeoxy-glucose

FGF	Fibroblast growth factor
FGFR	Fibroblast growth factor receptor
FLIM	Fluorescence lifetime imaging microscopy
FRS2α	Fibroblast growth factor receptor substrate 2α
GLS	Glutaminase
GO analysis	Gene ontology analysis
H&E	Hematoxylin and Eosin
HBSS	Hanks balanced salt solution
HistoCAT	Histology topography cytometry analysis toolbox
HK2	Hexokinase 2
HS	Heparan sulfate
HSPGs	Heparan sulfate proteoglycans
LDH	Lactate dehydrogenase
IMC	Imaging mass cytometry
JOCK	Juxtaposition of chemical inducer of dimerization and Kinase 1
mCRPC	Metastatic castration-resistant prostate cancer
MPC1	Mitochondrial pyruvate carrier 1
mpMRI	Multiparametric magnetic resonance imaging
mRNA	Messenger RNA
NADH	Nicotinamide adenine dinucleotide
NE	Neuroendocrine cells
OCR	Oxygen consumption rate

Oligo	Oligomycin
optoR1	Optically controlled FGFR1
OXPHOS	Oxidative phosphorylation
PCa	Prostate cancer
PD-1	Programmed death-1
PDH	Pyruvate dehydrogenase
PDHc	Pyruvate dehydrogenase complex
PD-L1	Programmed death-ligand 1
PDP1	Pyruvate dehydrogenase phosphatase
PEI	Polyethylenimine
PER	Proton efflux rate
PET/CT	Positron emission tomography-computed tomography
PIN	Prostatic intraepithelial neoplasia
PLCγ	Phosphoinositide phospholipase C gamma
PMSF	Phenylmethylsulfonyl fluoride
PSA	Prostate-specific antigen
RNA-seq	RNA-sequencing
Rot/AA	Rotenone/antimycin A
scRNA-seq	Single-cell RNA sequencing
sgRNA	Single guide RNA
SYP	Synaptophysin
TAK1	Transforming growth factor-β-activated kinase 1

TCA cycle	Tricarboxylic acid cycle
TME	Tumor microenvironment
TRAMP	Transgenic adenocarcinoma of the mouse prostate
T_{reg}	Regulatory T cells
TSP	3-(trimethyl−silyl)propionic acid-d4

TABLE OF CONTENTS

Page

LIST OF FIGURES

Page

LIST OF TABLES

Page

LIST OF EQUATIONS

Page

CHAPTER I

INTRODUCTION AND LITERATURE REVIEW

Prostate cancer

Prostate cancer (PCa) is the most common malignancy and the second leading cause of cancer death in males [1]. The progression of PCa is a long multiple-step process that usually transforms a lesion from slow-growing, androgen-sensitive to fast-growing, hormone-independent [2]. The glandular epithelium and supporting stroma constitute the two compartments of the prostate [3]. Normal prostate consists of three cell types: luminal cells (expressing cytokeratin 8, cytokeratin 18, CD57, and androgen receptor (AR)), basal cells (mostly AR negative, anchoring the epithelium to the basement membrane, which express cytokeratin 5, cytokeratin 14, CD44, and P63), and neuroendocrine cells (NE) that are AR negative, account for ~1% of epithelial cell population, express synaptophysin (SYP) and chromogranin A (CgA) [4]. Most PCa initiates with benign prostatic hyperplasia (BPH) accompanied by increased stromal and epithelial cells and progresses to prostatic intraepithelial neoplasia (PIN), which is usually characterized by luminal epithelial hyperplasia and decreased basal cells [5, 6]. The occurrence of high-grade PIN, as the precursor of prostatic carcinoma and usually marked by more apparent cytologic atypia and sometimes disruption of the basal layer, marks the transition phase from benign prostate lesions to invasive carcinoma [7, 8]. This stage embarks with loss of the basal cell layer where the localized PCa on the focal regions occurs, with much fewer distinguishable histopathological subtypes as in other epithelial tumors [5, 9]. Loss of androgen-responsiveness is often associated with the

advanced stage of PCa as defined by castration-resistant PCa (CRPC), which is metastatic and has no cure current. According to the statistics in 2021, the 5-year PCa survival rate drops sharply from 100% for early stages to 29% for advanced stages [10]. Consequently, early diagnosis and novel therapy strategy development are crucial to tackling this conundrum.

The early detection of PCa has been on the cusp of the over- and under-treatment tendency, and the current recommendations for the use of prostate-specific antigen (PSA) blood test are provided as part of a risk-adapted strategy to address it. The utilization of PSA blood test contributes to the dramatic spike in the PCa incidence trends in the early 1990s, followed by the gradual decline of mortality trends [10]. However, increasing evidence shows the limitations and ineffectiveness of PSA screening for late-stage patients with an increasing proportion of metastases at the time of diagnosis since 2011, which marks the stagnant era of the blood test screening and the urgent need for new biomarkers for early and precise diagnosis of PCa [11, 12]. With modern diagnostic techniques (such as multiparametric magnetic resonance imaging (mpMRI) guided biopsy) entering everyday clinical practice, evaluation standards for PCa diagnosis have been raised and refined by combining multiple tumor detection methods, which helps to improve the situation [13]. Besides, novel treatment may complement these new techniques in clinical practice for more precise and effective treatment of PCa patients.

Common strategies for PCa treatment

As a heterogeneous disease, primary PCa is often multifocal, which poses obstacles in the way of treatment [14]. The classical treatment landscape is highly reliant on sampling and grading of the lesion with molecular features. Radical prostatectomy, radiotherapy, and brachytherapy represent the most commonly used options (other than active surveillance) for patients with low- and intermediate-risk localized PCa [15-17]. Neoadjuvant and adjuvant hormone treatment ADT (androgen-deprivation therapy) is usually reserved for high-risk localized, hormone-naïve metastatic PCa and non-metastatic CRPC [17, 18], while chemotherapy stands for the first- and second- lines of metastatic CRPC (mCRPC) therapy [17, 19]. The drugs approved by the Food and Drug Administration (FDA) for PCa are listed in **Table 1**.

Table 1 FDA approved drugs commonly used for PCa

Name	US brand name	Mechanism
Abiraterone	Yonsa; Zytiga	Suppresses androgen synthesis by CYP17A [20]
Apalutamide	Erleada	Inhibits AR signaling [21]
Cabazitaxel	Jevtana	Promotes tubulin assembly and stabilizes microtubules [22]
Darolutamide	Nubeqa	Inhibites AR signaling [23]
Docetaxel	Tzxotere	Inhibits microtubule depolymerization [24]
Enzalutamide	Xtandi	Inhibits AR signaling [25]

PCa has an "immune cold" TME

To date, immunotherapy has been widely used to treat multiple cancers. However, PCa patients respond poorly to immunotherapies. Currently, the cancer vaccine Sipuleucel-T is the only FDA-approved immunotherapy treatment for PCa, which significantly improves the survival rate of PCa patients [26, 27]. Despite the remarkable success of Sipuleucel-T in clinical trials, it is only effective for a relatively small fraction of PCa patients [28, 29]. Novel strategies are urgently needed to improve PCa immunotherapy.

Most immunotherapy studies for PCa mainly focused on the immune checkpoint inhibitors (CPIs), which target the regulatory proteins of the immune response, including (but not limited to) programmed death-1(PD-1), programmed death-ligand 1 (PD-L1), and cytotoxic T-lymphocyte-associated protein 4 (CTLA-4). Despite that some single-agent therapies showed a durable response in a small cohort who may have benefitted from genomic profiling [30], the majority of these clinical trials ended up dissatisfied (**Table 2**), suggesting that PCa is not a promising target for single-agent anti-checkpoint therapy. The ongoing attempts combining CPIs with other agents aim to break the deadlock (**Table 2**); however, the clinical outcomes remain modest so far, leaving CRPC as an "immune desert" to immunologists [31]. One of the most popular hypotheses of the "immune cold" phenotype of PCa is that the PCa TME consists of immunosuppressive cells and molecules that render it hostile to immune cells, which leads to poor infiltration, proliferation, and differentiation of T cells. Others believe that immune responses were hampered by the loss of mutation-associated neoantigens and immunogenicity, which contributes to the poor recognition of immune cells.

Table 2 Clinical trials of CPIs (single-agent and combination) for mCRPC

CPI name	Target	ClinicalTrials.gov Identifier	Phase
Ipilimumab	CTLA-4	NCT00861814 [32]	III
		NCT01057810 [33]	III
Pembrolizumab	PD-1	NCT02054806 [34]	Ib
		NCT02787005 [35]	II
Atezolizumab	PD-L1	NCT01375842 [36]	Ia
Atezolizumab/Cabozantinib	PD-L1/RTK	NCT03170960 [37]	I/II
Nivolumab/Ipilimumab	PD-L1/CTLA-4	NCT03061539 [38]	II

In summary, the advanced PCa has long been a formidable challenge for urologists. Current treatment strategies commonly used in clinical practice are usually limited by the androgen responsiveness, drug resistance, and "immunologically cold" TME. As a new approach, immunotherapy has failed to gain success in PCa as it does in other cancer types, which may be partly due to a "cold" TME. Understanding the underlying mechanism of PCa progression and the regulation of TME may help warm up the immunological microenvironment, and further facilitate the development of more therapy options and the acceleration of screening for an effective cure for advanced stages of PCa.

Resident and ectopic FGF signaling in the prostate and PCa

Fibroblast growth factor (FGF) signaling is one of the major pathways that serve as a key regulator in prostate development, maintenance, and function. However, ectopic FGF signaling is associated with initiation, progression, and metastasis of PCa [4, 39]. The signaling component of the mammalian FGF family consists of members that are grouped into five paracrine FGF (also called canonical) subfamilies, one endocrine FGF subfamily, and one intracellular FGF subfamily (**Table 3**), which usually (expect for the intracellular FGFs) signal through interacting with 4 FGF receptors (FGFR) in mammals. Generally, FGFR is composed of a ligand-binding ectodomain region with three immunoglobulin (Ig)-like domains; a single transmembrane domain that anchors the receptor to the plasma membrane; and an intracellular tyrosine kinase domain (**Figure. 1**). The interaction of FGFs and FGFRs is modulated by these encompassing Ig-loops: Ig-loop I serves as the auto-inhibitory role that lowers the affinity for ligands and heparin [40-42]; Ig-loop II is highly conserved and interacts with ligands and heparan sulfate (HS) proteoglycans (HSPGs), the cofactor for paracrine FGF signaling [43]; and Ig-loop III determines the alternative splicing and further contributes to signal specificity [44, 45]. The FGFR forms ligand-independent dimers that are associated with HSPG and maintain an inactive conformation. Binding with FGF ligands changes the conformation of the FGFR dimer and leads to receptor autophosphorylation in the cytosolic kinase domain, which changes the conformation of the auto-inhibitory loop and recruits downstream target proteins and turns on the downstream signaling pathways in a receptor- and cell-type specific manner [4].

Table 3 FGF subfamilies

Name	Members	Signaling type	Cofactor
Fgf1 subfamily	Fgf1; Fgf2;		
Fgf4 subfamily	Fgf4; Fgf5; Fgf6;		
Fgf7 subfamily	Fgf3; Fgf7; Fgf10; Fgf22;	Paracrine	Heparin/HS
Fgf9 subfamily	Fgf9; Fgf16 Fgf20;		
Fgf8 subfamily	Fgf8; Fgf17; Fgf18		
Fgf15/19 subfamily	Fgf15/19; Fgf21; Fgf23	Endocrine	α/β-Klotho
Fgf11 subfamily	Fgf11; Fgf12; Fgf13; Fgf14;	Intracellular	-

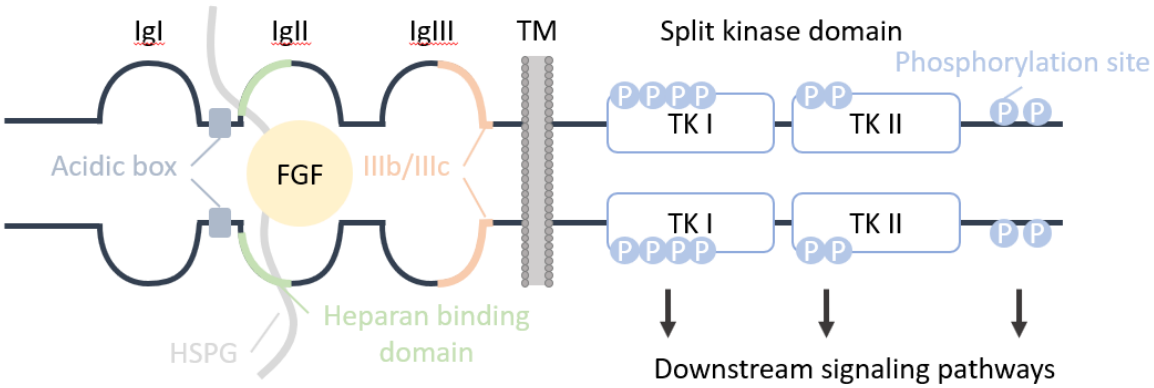

Figure 1 The FGFR signaling complex (Paracrine Fgf binding model)

FGFRs process three immunoglobulin-like loops (IgI; IgII; and IgIII), a transmembrane domain (TM), and the split tyrosine kinase domain (TKI and TKII). Activation of FGFR requires the binding of FGFs and HSPG chains around IgII and IgIII, and the phosphorylation of major tyrosine sites in the cytosolic region.

Despite that FGFRs share over 80% homology in primary sequence, their functions are quite distinct and sometimes oppose one another. Gain- and loss-of-function studies in mouse models revealed the requirement of FGF/FGFR signaling in

prostate development, homeostasis, and PCa progression in multiple directions, and the acquisition of FGFR1 expression in epithelial cells is usually highlighted among others [4, 46]. FGFR1 amplification and ectopic expression are common in multiple cancer types, including PCa [47]. The upregulation of Fgfr1 has been conclusively demonstrated in human prostate carcinoma and contributes to the short survival time in castrate-resistant PCa (CRPC) [48-50]. Activation of FGFR1 leads to time-dependent prostate lesions ranging from low-grade PIN to late-stage carcinoma in both FVB mice [51, 52] and the Juxtaposition Of Chemical inducer of dimerization and Kinase 1 (JOCK1) transgenic mouse model [53, 54]. Prostate-specific deletion of *Fgfr1* in the prostate epithelium leads to smaller tumors with less aggressive, slower tumor growth, and longer survival in the TRAMP (transgenic adenocarcinoma of the mouse prostate) model, suggesting that aberrant Fgfr1 is sufficient and sufficient for initiation and progression of PCa [55]. However, the underlying mechanism of how FGFR1 promotes PCa progression is still not clear. Multiple explanations diverge from each other, and most of them cover the aspects of both canonical and non-canonical downstream signaling pathways (**Figure. 2**).

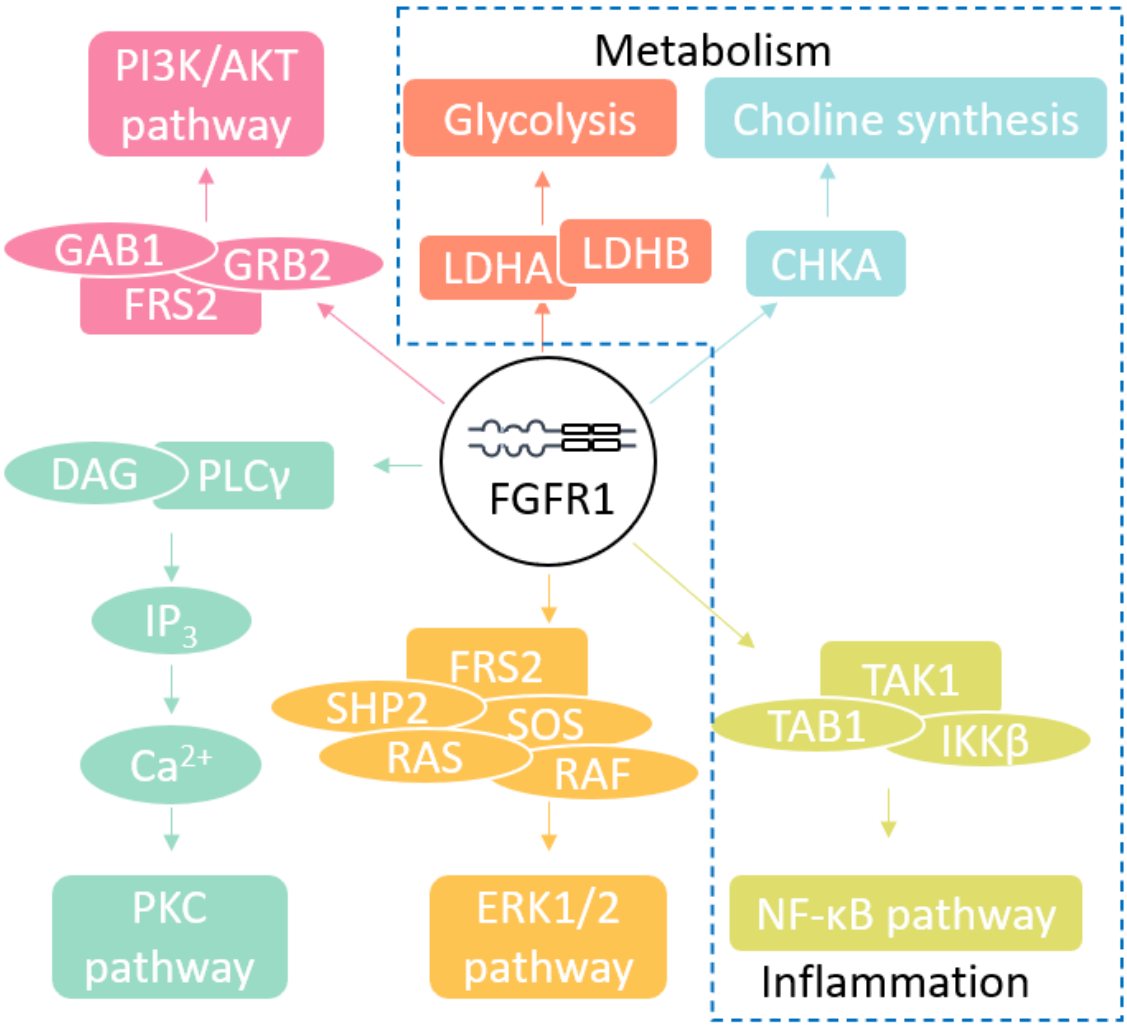

Figure 2 Simplified downstream signaling pathways of FGFR1

Canonical- and non-canonical (dashed blue line) downstream pathways of FGFR1.

There are three classical canonical FGFR1 downstream signaling pathways: the PI3K/AKT pathway and the ERK1/2 pathway activate following FGF receptor substrate 2α (FRS2α) recruitment to the phosphorylated receptor, and the PKC pathway becomes activated through phosphoinositide phospholipase C gamma (PLCγ) recruitment. These pathways contribute to a broad spectrum of cellular events, such as proliferation,

migration, angiogenesis, and apoptosis in PCa cells [56]. In addition to the common downstream pathways, increasing evidence reveals several non-canonical downstream pathways of FGFR1 that prevail in PCa cells. Ectopic FGFR1 augments NF-κB signaling by suppressing the proteasome-mediated degradation of transforming growth factor-β-activated kinase 1 (TAK1) in PCa cells and further reducing inflammation [57]. A recent report found that ablation of FGFR1 downregulates CHKA (Choline kinase α), as the first enzyme in de novo synthesis of phosphatidylcholine, and further suppresses PCa progression [58]. Finally, another critical non-canonical pathway that has been brought to light is aerobic glycolysis, which will be discussed in the following section.

Ectopic FGFR1 reprograms cell metabolism in PCa

The deregulation of cellular energy metabolism is one of the emerging hallmarks of cancer [59]. At the center of the energy metabolic network lies the glucose-dependent pathways, which allow for energy to be harnessed in the form of adenosine triphosphate (ATP) through oxidative phosphorylation (OXPHOS) in the mitochondria and by aerobic glycolysis happens in the cytosol [60]. Most mammalian cells take up glucose by glucose transporters (GLUT family) and metabolize it to pyruvate through a multi-step process known as glycolysis [61]. In normal (quiescent) cells, the glycolysis-derived pyruvate is primarily transported into mitochondria for decarboxylation by pyruvate dehydrogenase (PDH), which generates acetyl-CoA and starts the initial phase of the tricarboxylic acid cycle (TCA cycle). The completion of the TCA cycle leads to the generation of ATP and the two electron carriers, nicotinamide adenine dinucleotide (NADH) and flavin adenine dinucleotide ($FADH_2$), to feed the electron transport chain

in mitochondrial membrane to generate large quantities of energy (ATP) for various of cellular events [62]. This intricate process is known as OXPHOS. Unlike cells in normal tissues that generate energy primarily via OXPHOS, cancer cells reprogram the metabolism and preferably use glycolysis even under normoxia condition (designated aerobic glycolysis) to convert pyruvate to lactate via lactate dehydrogenase (LDH), which is referred as the Warburg effect [63, 64].

The metabolism reprograming from OXPHOS to aerobic glycolysis usually results from a composite series of responses from both cells and the TME [65] and plays a critical role in the cell growth machinery. Aerobic glycolysis is less efficient at generating ATP compared to OXPHOS but can provide sufficient metabolites as building blocks for cancer to meet the requirements for quick growth. The whole body FDG (^{18}F-fluorodeoxy-glucose)-PET/CT (Positron emission tomography-computed tomography) scan on a cohort of 6128 patients in 2015 showed no significant difference in glucose uptake between malignant and benign lesions [66]. Magnetic resonance imaging (MRI) of the TRAMP mice with normal prostate, low-grade, high-grade, and metastatic tumors showed that lactate increased in low-grade tumors and high-grade tumors, but gently dropped back in metastatic stages [67]. This is supported by metabolic imaging with the injection of [1-^{13}C] pyruvate on 12 PCa patients, which showed increased hyperpolarized lactate in tumor tissues with a higher Gleason score, suggesting that increased aerobic glycolysis may accompany PCa progression [68]. Meanwhile, a recent report that measured the OXPHOS in paired benign and malignant tissues from 50 PCa patients revealed the decreased OXPHOS capacity in high-grade

PCas compared to low-grade tumors, with decreased relative respiration [69]. Taken together, these data suggest that metabolic reprogramming from OXPHOS to aerobic glycolysis occurs during PCa progression, and targeting these metabolic pathways may yield a potential candidate for PCa treatment.

The causes and underlying mechanism for such a metabolic phenotype in PCa cells remain to be further clarified. In one hypothesis, low nutrition and oxygen concentrations commonly found in the TME could be responsible for cancer cells to choose aerobic glycolysis, and more importantly, the intermediates derived by aerobic glycolysis are in demand for macromolecular synthesis and survival [70]. Another explanation preferably links the TME alteration derived by metabolic reprogramming together with the immunosuppression [71, 72]. The general consequence of metabolic reprogramming in cancer cells is the increase in cancer-derived lactate and the scant nutrition and oxygen within the TME, all of which contribute to immune evasion by inhibiting immune cell cytotoxicity and proliferation [73]. A recent report found that lactate exhibits suppressive effects on T cell proliferation in a pH-independent manner, and it functions through the lactate-induced reductive stress accompanied by a shift from NAD^+ to NADH [74]. Lactate within the TME promotes FoxP3-mediated T cell polarization towards T_{reg} (regulatory T cells), which assist immune escape and sustain cancer malignancy [75]. These reveal the potential of warming up the TME in PCa via reducing levels of tumor-derived lactate.

However, aerobic glycolysis and OXPHOS pathways also are required for the infiltration, proliferation, and function of immune cells. Therefore, there is a major

hindrance to using metabolic inhibitors directly to decrease lactate accumulation in the TME. Recent studies reveal that ectopic expression of FGFR1 regulates the expression of 2 subunits of lactate dehydrogenase (LDH) by increasing the phosphorylation of LDHA as well as the methylation of the Ldhb promoter, leading to decreased lactate production and reprogramming from oxidative phosphorylation to aerobic glycolysis in PCa [76]. Genetically knockdown of *Fgfr1* downregulates HK2 (one of the rate-limiting glycolytic enzymes) at the protein and RNA levels in lymphatic endothelial cells [77]. These findings suggest the possibility of blocking FGFR1 as an alternative way to specifically decrease tumor-derived lactate, and further reduce the immune suppressiveness of the PCa TME.

To summarize, increasing evidence shows that the ectopic FGFR1 signaling contributes to PCa progression via a complicated network effect including but not limited to tumor angiogenesis, apoptosis, invasion, metastasis, inflammation, and metabolism, and suppression of FGFR1 signaling may serve as a candidate target for developing novel strategies for CRPC [4].

CHAPTER II

MATERIALS AND METHODS

Cell culture

HEK293T and human PCa cell line DU145 cells were cultured in Dulbecco's modified eagle's medium (DMEM, Gendepot, #CM001), supplemented with 10% fetal bovine serum (FBS, Gendepot, #F0900), 100 units/mL of penicillin and 100 µg/mL of streptomycin (PS, Gendepot, #CA005) in an incubator maintaining 5% CO_2. Human T lymphocyte Jurkat cells were cultured in RPMI-1640 medium (VWR, #12001-592) supplemented with 10% FBS and 1% PS in 5% CO_2.

Generation of *FGFR1* knockout cell lines

The clustered regularly interspaced short palindrome repeats (CRISPR)–associated nuclease Cas9 system was used to knockout the *FGFR1* alleles in DU145 cells. The single guide RNA (sgRNA) sequence (5'- CACATACCAGCTGGATGTCG -3') was designed and inserted into the LentiCRISPRv2 vector (Addgene, #52961) with a puromycin resistance marker (puro) following the protocol as previously described [78, 79]. The targeted plasmid LentiCRISPRv2-*FGFR1* was then co-transfected into HEK293T cells with packaging plasmids psPAX2 (Addgene, #12260) and pMD2.G (Addgene, #12259) through polyethyleneimine (PEI) to generate the lentiviral particles. The supernatant was collected after 24 hours and stored at 4°C prior to use. DU145 cells were infected via filtered supernatant containing lentivirus particles and selected by puromycin. The single-clonal expansion was performed to select targeted clones with relatively high knockout efficiency.

Generation of optoR1 overexpression cell lines

The fragment of the optically controlled FGFR1 (optoR1) consisting of the cytosolic regions of FGFR1; the photosensory protein cryptochrome 2 (CRY2PHR); and the fluorescent protein mCitrine as described previously [80] was cloned into the pWPXL vector. The QuikChange Lightning Multi Site-Directed Mutagenesis Kit (Agilent, #210513) was used for generating optoR1 D623A mutant plasmid, with primer sequence (5'- CATACACCGAGCCCTGGCAGCCAGG -3') designed following the manufacturer's protocol. The targeted plasmid (pWPXL-optoR1 WT and pWPXL-optoR1 D623A, respectively) was then co-transfected into HEK297T cells with packaging plasmids psPAX2 and pMD2.G through polyethyleneimine (PEI) to generate the lentiviral particles. DU145$^{\Delta R1}$ cells were infected and enriched by FACs and polyclonal expansion.

Seahorse real-time cell metabolic analysis

The Seahorse XF Cell Mito Stress Test (Agilent, #103015-100), Seahorse XF Glycolytic Rate Assay (Agilent, #103344-100), Seahorse XF Real-Time ATP Rate Assay (Agilent, #103592-100), and Seahorse XF Mito Fuel Flex Test (Agilent, #103260-100) kits were used to evaluate the metabolism changes separately via the Seahorse XF96 Analyzer (Agilent Technologies Inc., Santa Clara, CA, USA) following the manufacturer's manuals. DU145 cells were seeded at 15,000 cells/well in Seahorse XF96 tissue culture microplates. Oxygen consumption rate (OCR) and extracellular acidification rate (ECAR) were measured during each assay and were used to calculate the metabolic index, including proton efflux rate (PER), metabolic pathway dependency

and capacity of the cells. The FGFR1 inhibitor AZD4547 (SelleckChem, #S2801, 100 ng/mL) was added to the medium 6 hours prior to the assay as indicated. The activation of the optoR1 system was accomplished by pulsed blue light stimulation (5 minutes on and 5 minutes off) for 24 hours. Cells were incubated in normal air at 37°C with Seahorse XF DMEM Medium (Agilent, #103575) for 1 hour before measurement. The concentrations of compounds injected during the assay are listed in **Table 4**. Data was normalized by the cell number measured in individual wells with DAPI (VWR, #89139-054) nuclear staining via Cytation5 (BioTek, Winooski, VT, USA). Metabolic parameters were calculated by OCA and ECAR as indicated in **Table 5**, which follows the manufacturer's instructions.

Table 4 Compounds used in Seahorse metabolic analysis

Assay	Compound	Final concentration
Mito stress test	Oligomycin	1.0 μM
	FCCP	1.0 μM
	Rot/AA	0.5 μM
Glycolytic rate assay	Rot/AA	0.5 μM
	2-DG	50 mM
ATP rate assay	Oligomycin	1.5 μM
	Rot/AA	0.5 μM
Mito fuel flex test	BPTES	3.0 μM
	Etomoxir	4.0 μM
	UK5099	2.0 μM

Table 5 Metabolic parameter calculation

Name	Equation
Basal (Respiration)	(Last rate before Oligo) - (Min rate after Rot/AA)
Maximal Respiration	(Max rate after FCCP) - (Min rate after Rot/AA)
ATP production	(Last rate before Oligo) - (Min rate after Oligo)
Spare capacity	[(Max respiration) - (Basal respiration)] x 100%
Proton Leak	(Min rate after Oligo) - (Min rate after Rot/AA)
Coupling Efficiency	(ATP production) / (Basal respiration) x 100%
Basal (glycolysis)	Last glycoPER rate before Rot/AA
Compensatory (glycolysis)	Max glycoPER rate after Rot/AA
Post 2-DG acidification	Min glycoPER rate after 2-DG
PER	ECAR x Buffer factor x $Vol_{microchamber}$ x Kvol
glycoPER	PER – (OCR_{basal} – $OCR_{Rot/AA}$)
glycoATP production	glycoPER
mitoATP production	(OCR_{basal} – OCR_{Oligo}) x 2 x P/O ratio
ATP production rate	glycoATP production + mitoATP production

Western blot analysis

Cells were seeded in 6-well dishes at 30,000 cells/well. The activation of the optoR1 system was accomplished by continuous blue light stimulation for 20 minutes. Cells were lysed in radioimmunoprecipitation assay buffer (50 mM Tris-HCl, pH 7.4; 1 mM EGTA; 1mM phenylmethylsulfonyl fluoride; 1% Nonidet P-40; 0.25% sodium deoxycholate; 150 mM NaCl) supplemented with 1% Xpert phosphatase inhibitor cocktail solution (Gendepot, #P3200) and 1 mM PMSF (phenylmethylsulfonyl fluoride), and centrifuged at 10,000 g for 10 minutes to harvest protein. The concentrations of samples were quantified individually by Pierce™ BCA Protein Assay kit (Thermo Fisher, #23225). Lysates containing 25 μg protein were separated by SDS-PAGE and blotted onto PVDF (polyvinylidene difluoride) membranes. The membrane was incubated in 5% BSA for 1 hour and probed with the indicated antibodies as follows: Anti-FGFR1 (Abcam, #ab76464), 1:1,000; anti-ERK1/2 (CST, #9102S), 1:1,000, anti-phospho-p44/42 MAPK (pERK1/2) Thr202/Tyr204 (CST, #4376S), 1:1,000; anti-β-actin (Santa Cruz, #sc-47778), 1:2,000.

RNA-sequencing

Messenger RNAs (mRNA) with poly-A tails were enriched by NEBNext Poly(A) mRNA Magnetic Isolation Module (NEB, #E7490) and used for RNA-sequencing (RNA-seq) library preparation using NEBNext Ultra II Directional RNA Library Prep Kit for Illumina (NEB, #E7760). RNA-seq was performed via NextSeq™ 550 system (Illumina, CA). Quality control was ascertained by FastQC [81] and MultiQC [82]. The reads were transformed to FPKM (paired fragments per kilobase of transcript per million

mapped reads) and mapped via TopHat [83] and Cufflinks [83-87]. DEGs (Differentially expressed genes) were defined in $DU145^{Ctrl}$ and $DU145^{\Delta R1}$ cells by fold change ≥ 2 and FDR < 0.05. Enrichment analysis on DEGs was performed via GO analysis (Gene ontology analysis). The R scripts were used to generate the volcano plot, heatmap, and dot plots for DEGs.

The NAD(P)H and FAD fluorescence lifetime imaging

The fluorescence images and lifetime images were acquired through Fluorescence lifetime imaging microscopy (FLIM, 3i Intelligent Imaging Innovations, Inc., Denver CO, USA) and analyzed as described previously [88, 89]. The cyanide perturbation assay was performed in DU145 cells with 5-minute exposure to 4 mM cyanide (Sigma, #380970) in a 5% CO_2 incubator prior to validation of the imaging protocol to prevent potential bias from chemical inhibition of OXPHOS [90]. The NAD(P)H and FAD images were acquired under excitation at 750 nm and 890 nm, respectively. The fluorescence lifetime parameters, including the short lifetime (τ_1), the long lifetime (τ_2), the proportional component of short lifetime (α_1), the amplitude-weighted lifetime (τ_m), and the redox ratio (NADH/(NADH+FAD)) were computed by the equations as previously described [89].

Conditioned medium collection and cell proliferation assay

Conditioned medium (CM) was collected 24 hours after changing fresh DMEM medium from confluent DU145 cells, and was filtered through a 0.22 μm filter (VWR, #76479-030) prior to use. Jurkat cells were seeded into 96-well plates and were cultured in the absence or presence of 10% CM for five days. Lactic acid (Sigma, #L1750)

prepared by serial dilution (30 mM; 10 mM; 3.3 mM; and 1.1 mM) was added 24 hours after seeding. The cell densities from Day 1 to Day 5 were measured through absorbance with CCK-8 (Cell Counting Kit-8, Dojindo, #CK04) on a Synergy H1 Hybrid Multi-Mode Reader (Agilent Technologies Inc., Santa Clara, CA, USA).

Animal housing and breeding

TRAMP transgenic mice with a mixed background were housed under the Program of Animal Resources of the Institute of Biosciences and Technology in accordance with the principles and procedures of the Guide for the Care and Use of Laboratory Animals. TRAMP mice were bred and genotyped as described previously [55, 91-93]. Conditional ablation of *Fgfr1* was achieved via crossing TRAMP mice, ARR_2PBi-*Cre* mice, and $Fgfr1^{loxP/loxP}$ mice as described previously [55]. The PCa tissues and/or the prostates were harvested from mice at the age of 28-32 weeks old, with all experimental procedures approved by the Institutional Animal Care and Use Committee.

***In vivo* treatment**

The tumor growth of the mice was monitored by ultrasound imaging biweekly (or weekly) starting at the age of 26- 28 weeks old using the preclinical imaging platform Vevo 3100 Imaging System (FUJIFILM VisualSonics, Inc., Toronto, Ontario, Canada) follow the protocol as described previously [94, 95]. The ultrasound coupling gel Aquasonic 100 (Parker Laboratories, Inc., #01-50) was applied to the depilated skin of the anesthetized mice to facilitate the image acquisition in transverse and sagittal orientation. Mice were randomized into treatment groups. The first injection was given when tumor size reached around 1 mm^3 as measured by ultrasound imaging. For

treatment protocols performed in mice with and without conditional ablation of *Fgfr1*, monoclonal anti-PD-1 antibody (BioXcell, #BE0146) was given intraperitoneally every two days at 200 mg/dose diluted in InVivoPure pH 7.0 Dilution Buffer (BioXcell, #IP0070) as the manufacture recommended. Control animals received InVivoMAb rat IgG2a isotype control (BioXcell, #BE0089). For combination treatment assessed in TRAMP mice, the administration scheme is listed in **Table 6**. The FGFR1 inhibitor AZD4547 (SelleckChem, #S2801) was given at 5 mg/kg body weight intraperitoneally. The tumors and/or prostate tissues were collected for further analysis after treatment. Tumor volume after the treatment was calculated using the formula below as previously described [96], where V stands for tumor volume after treatment; W and L represent the width and length of the tumor, respectively.

Equation 1 Tumor volume calculation

$$\boldsymbol{V = (W^2 \times L)/2}$$

Table 6 Treatment protocol for AZD4547 and anti-PD-1 combination

Group	PBS	AZD4547	Anti-PD-1	Combined
Day 1	PBS	AZD4547	PBS	AZD4547
Day 2	IgG2a	IgG2a	Anti-PD-1	Anti-PD-1
Day 3	PBS/IgG2a	AZD4547/IgG2a	PBS/anti-PD-1	AZD4547/anti-PD-1
Day 4	No injection			
Day 5	PBS/IgG2a	AZD4547/IgG2a	PBS/anti-PD-1	AZD4547/anti-PD-1
Day 6	No injection			
Day 7	PBS/IgG2a	AZD4547/IgG2a	PBS/anti-PD-1	AZD4547/anti-PD-1
Day 8	No injection			
Day 9	PBS/IgG2a	AZD4547/IgG2a	PBS/anti-PD-1	AZD4547/anti-PD-1
Day 10	No injection			
Day 11	PBS/IgG2a	AZD4547/IgG2a	PBS/anti-PD-1	AZD4547/anti-PD-1
Day 12	No injection			
Day 13	PBS/IgG2a	AZD4547/IgG2a	PBS/anti-PD-1	AZD4547/anti-PD-1
Day 14	Sample collection			

Histology and immunostaining

Mouse tissues were fixed, dehydrated, paraffin-embedded, and sectioned into 5 μm tissue sections after harvest. H&E (Hematoxylin and Eosin) staining was performed following the standard protocol. For immunofluorescence staining, antigen retrieval was conducted in citrate buffer (Citric acid 10 mM; and 0.05% Tween 20; pH 6.0) treatment under low pressure for 20 minutes. Slides were blocked with 1% BSA (Bovine Serum Albumin, Gendepot, #A0100) for 20 minutes and incubated with primary antibodies diluted in 1% BSA at 4°C overnight. The primary antibodies used are: Anti-FGFR1 (Abcam, #ab10646), 1:200; CD8α (CST, #98941), 1:200, which was conjugated with anti-rabbit Alexa Fluor 488 (ThermoFisher, #A-21206). The images were acquired using a W1-Yokogawa-Ti2-Nikon Spinning Disk Confocal microscope (Nikon, Minato, Tokyo, Japan) and analyzed by NIS-Elements Viewer software following the manufacturer's protocol.

Real-time PCR

Total RNA was extracted using the RiboZol™ RNA extraction reagent (VWR, #97064-950). The cDNA was synthesized by SuperScript™ III Reverse Transcriptase (ThermoFisher, #18080044) with random primers (ThermoFisher, #48190011) and used for real-time PCR analysis using the Fast SYBR™ Green Master Mix (ThermoFisher, #4385612) following the manufacturer's protocol. The primers used are listed in **Table 7**. The data were analyzed by the 2^(-Delta Delta CT) method normalized by mouse β-actin as described previously [97].

Table 7 Primers for real-time PCR

Gene name		Sequence (5' - 3')
Mouse *Fgfr1*	Forward	CACCAGACACTGTCCACCC
	Reverse	TTCAAACTGACCCTTGCCTC
Mouse *CD8*	Forward	TACTACCAAGCCAGTGCTGC
	Reverse	TCACAGGCGAAGTCCAATCC
Mouse *β-actin*	Forward	CACTGTCGAGTCGCGTCC
	Reverse	TCATCCATGGCGAACTGGTG

Flow cytometry analysis

Mouse tissues were excised and digested in the digestion medium containing 1 mg/ml Collagenase D (Sigma, #COLLD-RO) at 37°C for 6 hours, and passed through a 100 μM cell strainer (Greiner, #542000). Cells were resuspended in FACS buffer (5% FBS and 1% BSA in PBS) and incubated with primary antibodies for 30 minutes in the dark as indicated: PE anti-mouse CD8α (Biolegend, #100707), 1:800; APC anti-mouse CD3α (Biolegend, #100236), 1:400. The samples were transferred into round-bottom test tubes with a cell strainer snap cap (ThermoFisher Scientific, #08-771-23). Flow cytometry data were acquired by a BD Biosciences LSRII analytical flow cytometer (BD Bioscience, Franklin Lakes, NJ, USA) and analyzed by FlowJo software v10.5.3 following the manufacturer's protocol.

Imaging mass cytometry

Mouse tissues were fixed, dehydrated, paraffin-embedded, and sectioned into 5 μm tissue sections after harvest. Antibodies were conjugated with designated metal isotopes by Maxpar antibody labeling kits (Fluidigm, San Francisco, CA, USA). Antigen retrieval was conducted in citrate buffer (Citric acid 10 mM; and 0.05% Tween 20; pH 6.0) at 95°C for 20 minutes. Slides were incubated with Cell-ID^{TM} Intercalator (Fluidigm, #201192A) containing iridium (^{191}Ir and ^{193}Ir) for 5 minutes for nuclear staining. Section ablation was performed by the Hyperion^{TM} Imaging System (Fluidigm, San Francisco, CA, USA). IMC data was segmented by BordenmillerGroup ImcSegmentationPipeline and Spectre workflow [98] and visualized by Histology topography cytometry analysis toolbox (HistoCAT) [99]. R scripts were used to generate tSNE plots. The cellular markers used to define cell types manually [100] are listed in **Table 8**.

Table 8 Marker for cell type definition in IMC analysis

Cell type	Marker
T cell	CD8α
Macrophage	F4/80; CD86; CD11b
MDSC	Ly6C; Ly6G
Endothelial cell	Endomucin
Dendritic cell	CD11c
Others	N/A

Single-cell RNA-sequencing analysis

Single-cell RNA-sequencing (scRNA-seq) data from patient samples were downloaded from NCBI's GEO Database (Gene Expression Omnibus) [101, 102], which are accessible through GSE176031 [103]. Data analysis was performed on R v4.1.2 with the Seurat package v4.0.6 [104]. The expression matrix was visualized through UMAP by R [105]. The cellular markers used to define cell types manually [100] are listed in **Table 9**.

Table 9 Marker for cell type definition in scRNA-seq analysis

Cell type	Marker
Epithelial cell	EPCAM; KRT8; CDH1
Fibroblast	DCN; TNFAIP6; APOD; FBLN1
Myeloid cell	CD14; CD68; AIF1; CSF1R
Mast cell	MS4A2; ENPP3; PCER1A; KIT
Endothelial cell	ENG; CLDN5; VWF; CDH5
Basal cell	KRT5; TP63
T cell	CD2; CD3D; CD3E; CD3G
Myofibroblast	MYH11; GJA4; RGS5; MT1A

Statistical analysis

The two-tailed t-test was performed by GraphPad Prism 9.2.0 (GraphPad Software, San Diego) for statistical analysis with a significance threshold set as $p < 0.05$ (*); $p<0.01$ (**); and $p<0.005$(***). Error bar indicates the standard deviation.

CHAPTER III

RESULTS AND CONCLUSIONS

Ablation of FGFR1 reverses metabolic reprogramming in PCa cells

The ectopic expression of Fgfr1 has been demonstrated in human prostate carcinoma and contributes to the short survival time in CRPC [48-50]. A recent report revealed that expression of Fgfr1 increased PCa bone metastasis in CB17.SCID mice [106], demonstrating the critical importance of FGFR1 signaling during PCa progression. However, conclusive evidence is still needed for the underlying mechanism of how FGFR1 promotes PCa progression. Multiple explanations diverge from each other, and one of these theories focuses on the potential crosstalk between the FGFR1 signaling pathway and metabolic pathways. Recent reports reveal that FGFR1 regulates some of the key enzymes in glycolysis, including LDH and HK2, suggesting that FGFR1 signaling may promote aerobic glycolysis [76, 77]. Also, increased oxygen consumption was observed in MEF and DU145 cells upon FGFR1 ablation, suggesting that ablation of FGFR1 signaling suppressed mitochondrial activity [76]. [1-^{13}C] pyruvate advanced imaging experiments demonstrate a clinical linkage between decreased lactate and high tumor grades, suggesting that aerobic glycolysis might accompany PCa progression [66-68]. While the decreased OXPHOS capacity in high-grade PCa compared to low-grade tumors was recently reported in PCa patient samples, suggesting that decreased mitochondrial respiration was relevant to PCa progression. Taken together, we hypothesize that ablation of FGFR1 reverses metabolic reprogramming by suppression of aerobic glycolysis and promoting OXPHOS, and thus suppresses PCa progression.

Loss of FGFR1 signaling increases mitochondrial respiration

To investigate how ectopic FGFR1 signaling is involved in metabolic reprogramming in PCa, the CRISPR/Cas9 gene-editing system was used to generate Fgfr1 ablation cells ($DU145^{\Delta R1}$). Quantitative Seahorse flux analysis (Agilent Technologies Inc., Santa Clara, CA) was used to analyze cell metabolism changes. The oxygen consumption rate (OCR) was quantified as an indicator of cellular oxidative phosphorylation. A significant increase in mitochondrial respiration, as reflected in increased basal OCR and maximal respiration, was observed in $DU145^{\Delta R1}$ cells (**Figure 3A** and **3B**), which suggested that ablation of FGFR1 signaling not only elevated the basal level OXPHOS but also increased the mitochondrial respiration capacity. A moderate increase in the ATP production due to oxygen consumption together with a comparable coupling efficiency indicated that a similar fraction of mitochondrial respiration was dedicated to energy synthesis in $DU145^{Ctrl}$ and $DU145^{\Delta R1}$ cells, but more ATP was produced in $DU145^{\Delta R1}$ cells (**Figure 3B** and **3C**), suggests that the efficiency of mitochondrial respiration was increased upon FGFR1 ablation. The spare capacity, having a similar tendency, was moderately increased in $DU145^{\Delta R1}$ cells compared to $DU145^{Ctrl}$ cells (**Figure 3B**). This suggested that mitochondria in $DU145^{\Delta R1}$ cells are more capable of responding to severe cellular stress and workload to meet extra energy demand. A slightly increased proton leak was also observed in $DU145^{\Delta R1}$ cells. Taken together, ablation of FGFR1 increased OXHPOS in DU145 cells.

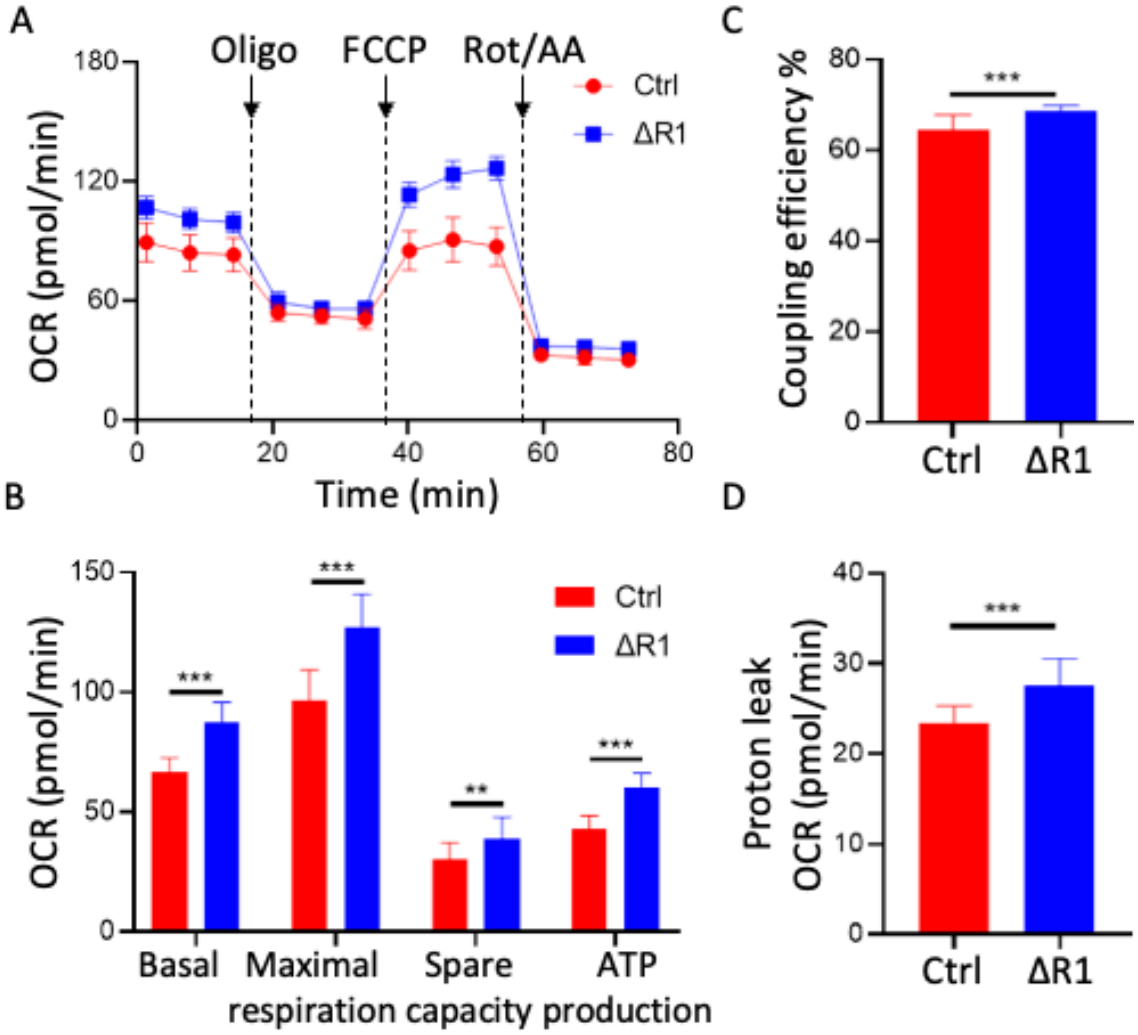

Figure 3 Ablation of FGFR1 increases OXPHOS in DU145 cells.

A) OCR measured in DU145^{Ctrl} (n=15) and DU145$^{\Delta R1}$ cells (n=15) with the addition of Oligo, FCCP, and Rot/AA; B) Metabolic parameters calculated by OCR, including basal respiration, maximal respiration, spare capacity, and ATP production; C) Coupling efficiency calculated by OCR; and D) Proton leakage calculated by OCR. Ctrl, DU145^{Ctrl} cells; ΔR1, DU145$^{\Delta R1}$ cells. Error bars represent mean ± SEM. **p<0.01, ***p<0.001.

To validate if ectopic FGFR1 signaling suppresses OXPHOS in PCa cells, a 6-hour treatment with AZD4547 (a specific FGFR1 inhibitor functioning in an ATP-competitive manner [107]) was performed in DU145 cells before quantitative Seahorse XF Mito Stress analysis. Similar to FGFR1 ablation, treating the cells with AZD4547 also showed increased OXPHOS with basal respiration, maximal respiration, and ATP production (**Figure 4A** and **4B**). A significant reduction in spare capacity after short-term treatment with AZD4547 was observed (**Figure 4B**), which was probably due to inhibitor dynamics leading to upheaval stress in PCa cells. We did not see significant changes in either coupling efficiency or proton leak because of the short timeline of treatment (**Figure 4C** and **4D**). Overall, these data indicate that blocking the FGFR1 signaling pathway increases OXPHOS in DU145 cells, which is consistent with an increased OXPHOS upon FGFR1 ablation.

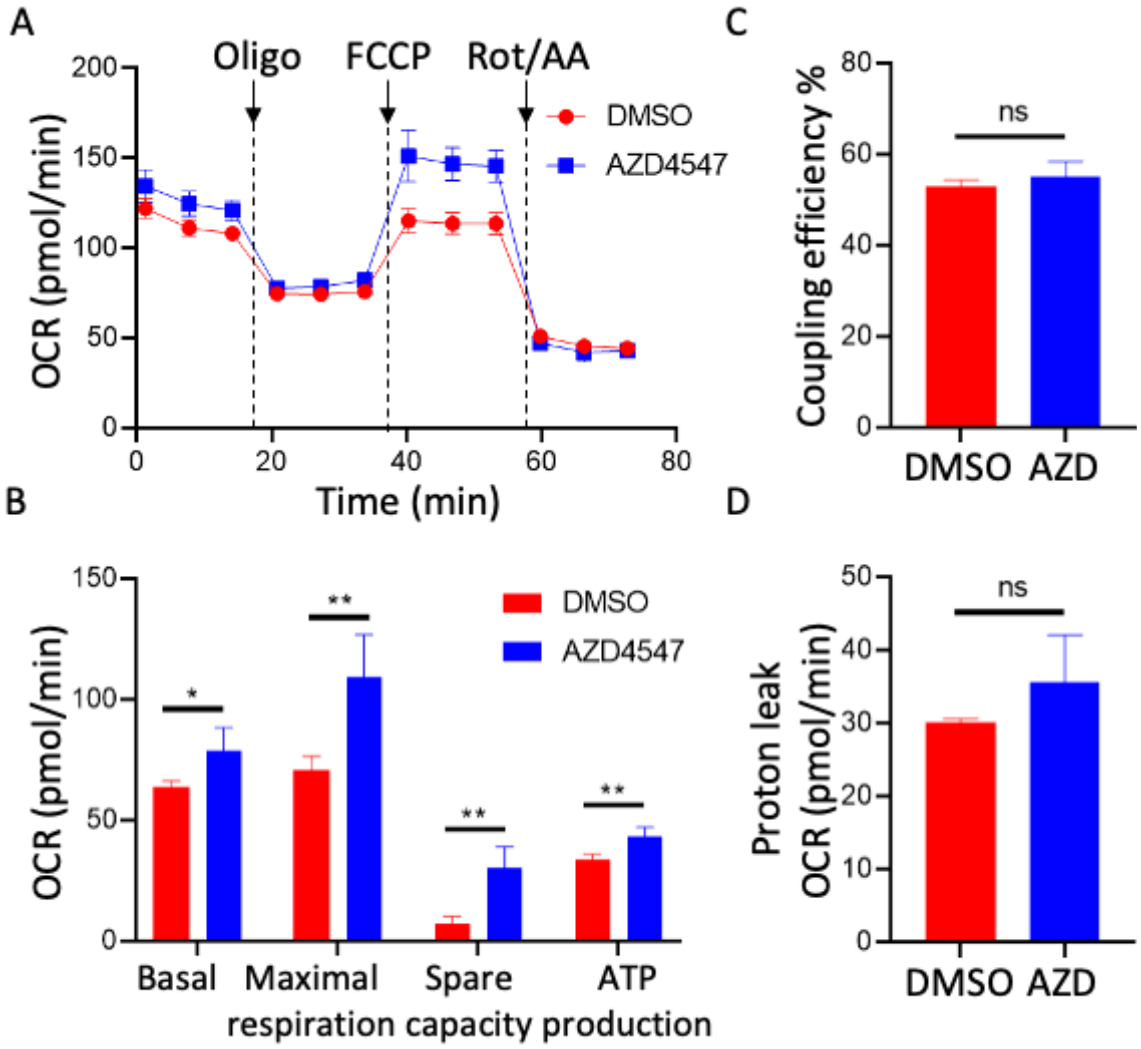

Figure 4 Blocking FGFR1 signaling increases OXPHOS in DU145 cells.

A) OCR measured in DU145 cells in the absence (n=4) or presence (n=4) of 100 ng/mL AZD4547 with the addition of Oligo, FCCP, and Rot/AA; B) Metabolic parameters calculated by OCR, including basal respiration, maximal respiration, spare capacity, and ATP production; C) Coupling efficiency calculated by OCR; and D) Proton leak calculated by OCR. DMSO, DU145 cells treated with 1% DMSO as the control for 6 hours; AZD and AZD4547, DU145 cells treated with AZD4547 for 6 hours. Error bars represent mean ± SEM. *p<0.05, ***p<0.01.

To address how ectopic FGFR1 promotes OXPHOS in PCa cells, we took advantage of the previously reported optically-controlled system optoR1 (consisting of the cytosolic regions of FGFR1 to remove endogenous ligand binding, the photosensory protein cryptochrome 2 (CRY2PHR) as an optogenetic module responding to blue light stimulation; and mCitrine as an intracellular fluorescent label [80]) and generated a DU145 cell line stably expressing the wildtype or kinase-dead mutant (D623A) of optoR1 (optoR1^{WT} and optoR1^{D623A}, respectively). Asp-623 is the catalytic base within the catalytic loops of the FGFR1 kinase domain [108], while mutation of D623A renders FGFR1 inactive through silencing the three-stage tyrosine autophosphorylation [109]. To validate the mutant function of optoR1^{D623A}, activation of classical downstream ERK signaling was measured by Western blot. The result showed increased pERK$^{T202/T204}$ in DU145$^{\Delta R1}$ cells exogenously overexpressing optoR1^{WT} but not in cells expressing the optoR1^{D623A} mutant after 20 minutes of continuous blue light stimulation (**Figure 5A**). We then measured the mitochondrial respiration of these two systems with long-term pulsed blue light stimulation (5 minutes on and 5 minutes off) for 24 hours, and found optoR1^{WT} dramatically decreased OXPHOS, as reflected in the basal respiration, maximal respiration, spare capacity and ATP production, in response to blue light stimulation, but not optoR1^{D623A} (**Figure 5B - 5F**). These suggest that blue light induced specific activation of FGFR1 signaling which suppressed OXPHOS in DU145 cells.

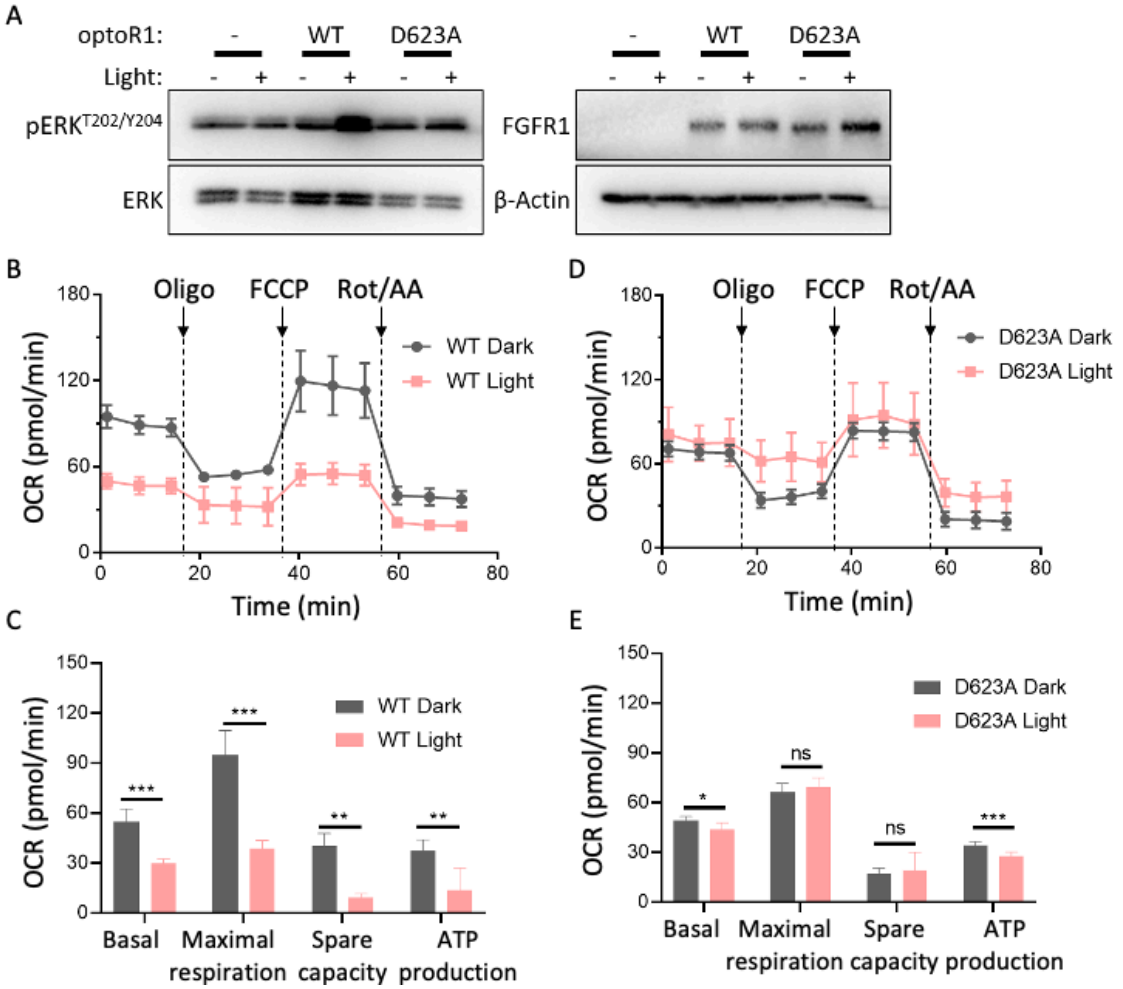

Figure 5 Blue light-induced activation of FGFR1 signaling suppressed OXPHOS in DU145 cells.

A) Western blot measurement of wildtype and kinase-dead mutant (D623A) of optoR1 in response to continuous blue light stimulation; B) OCR measured in DU145 cells overexpressing optoR1 wildtype in the dark (n=6) or with pulsed blue light stimulation (n=6); C) Metabolic parameters calculated by OCR in DU145 cells with optoR1 wildtype overexpression upon pulsed blue light stimulation; E) OCR measured in DU145 cells overexpressing optoR1 kinase-dead mutant (D623A) in the dark (n=5) or with pulsed blue light stimulation (n=5); E) Metabolic parameters calculated by OCR in DU145 cells with optoR1 kinase-dead mutant (D623A) overexpression upon pulsed blue light stimulation. Dark, control group without light stimulation for 24 hours prior OCR measurement; Light, light treatment either with continuously blue light for 20 minutes before Western blot, or 5 minutes on and 5 minutes off pulsed blue light for 24 hours before OCR measurement. Error bars represent mean ± SEM. *p<0.05, ***p<0.01.

Ablation of FGFR1 leads to increased redox ratio

To further understand how ablation of FGFR1 promoted metabolic reprogramming in PCa cells, we took advantage of a recent technology FLIM (fluorescence lifetime imaging) to measure the optical redox ratio in PCa cells. As the major electron donor (NADH) and acceptor (FAD) in OXPHOS, the autofluorescence exhibited by reduced NAD(P)H and FAD is widely used as indicators of cellular metabolism [89, 110]. The redox ratio calculated by NAD(P)H and FAD intensities represents the relative change rate of glucose catabolism to OXPHOS, where the reduction of NADH converting to NAD^+ together with increased FAD converting from $FADH_2$ result in a decreased redox ratio [111]. DU145 cells with or without cyanide treatment, which inhibits complex IV of the ETC (Electron transport chain), were imaged through Fluorescence lifetime imaging microscopy following the protocol as previously reported [89]. The cyanide perturbation assay allows the validation of the imaging protocol to prevent potential bias from chemical inhibition of OXPHOS [90]. The redox ratio (NADH/(NADH+FAD)) was plotted in **Figure 6**. The paired fluorescence lifetime images acquired for NADH and FAD were shown in **Figures 7A** and **7A**, respectively. The fluorescence lifetime parameters, including short lifetime (τ_1), long lifetime (τ_2), the proportional component of short lifetime (α_1), and the amplitude-weighted lifetime (τ_m) for NADH and FAD as calculated using the equation described in [89] were plotted in **Figure 7B** and **8B**.

The expected result under the cyanide perturbation assay as reported previously [90] was observed as the redox ratio (NADH/(NADH+FAD)) increased as NAD(P)H τ_m decreased in both $DU145^{Ctrl}$ and $DU145^{\Delta R1}$ cells. Both the short (τ_1, **Figure 7B**, top left)

and long (τ_2, **Figure 7B**, top right) lifetimes of NAD(P)H decreased in DU145$^{\Delta R1}$ cells, suggesting that the free- and protein-bound NADH were slightly reduced in DU145$^{\Delta R1}$ comparing to DU145^{Ctrl} cells. The drop of α_1 NAD(P)H was observed in DU145$^{\Delta R1}$ cells (**Figure 7B**, bottom left), suggesting that DU145^{ctrl} cells have a higher utilization rate of free NAD(P)H than that of DU145$^{\Delta R1}$ cells. The amplitude-weighted NAD(P)H lifetime (τ_m) remained comparable in DU145^{Ctrl} and DU145$^{\Delta R1}$ cells (**Figure 7B**, bottom right). We also observed slight decreases in both τ_1, τ_2, and τ_m, but increased α_1 of FAD in DU145$^{\Delta R1}$ cells (**Figure 8B**). More importantly, the redox ratio (NADH/(NADH+FAD)) increased (**Figure 6**), suggesting that the OXPHOS rate was increased in DU145$^{\Delta R1}$ cells.

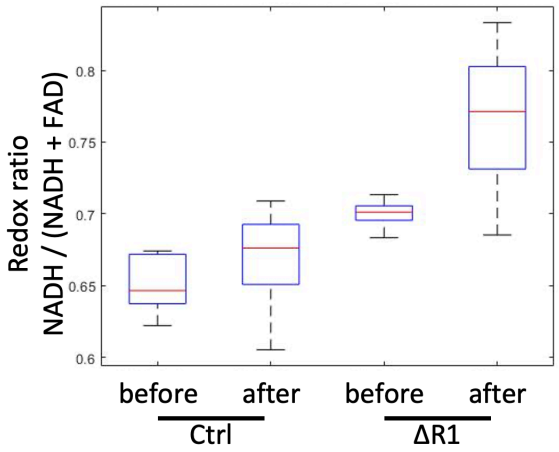

Figure 6 Redox ratio (NADH/(NADH+FAD)) in DU145 cells

Redox ratio (NADH/(NADH+FAD)) was mapped in the boxplot with median (red line inside the box) and the first and third quartiles. Before: control group without cyanide treatment; After: with 4 mM cyanide treatment for 5 minutes. Ctrl, DU145^{Ctrl} cells; ΔR1, DU145$^{\Delta R1}$ cells.

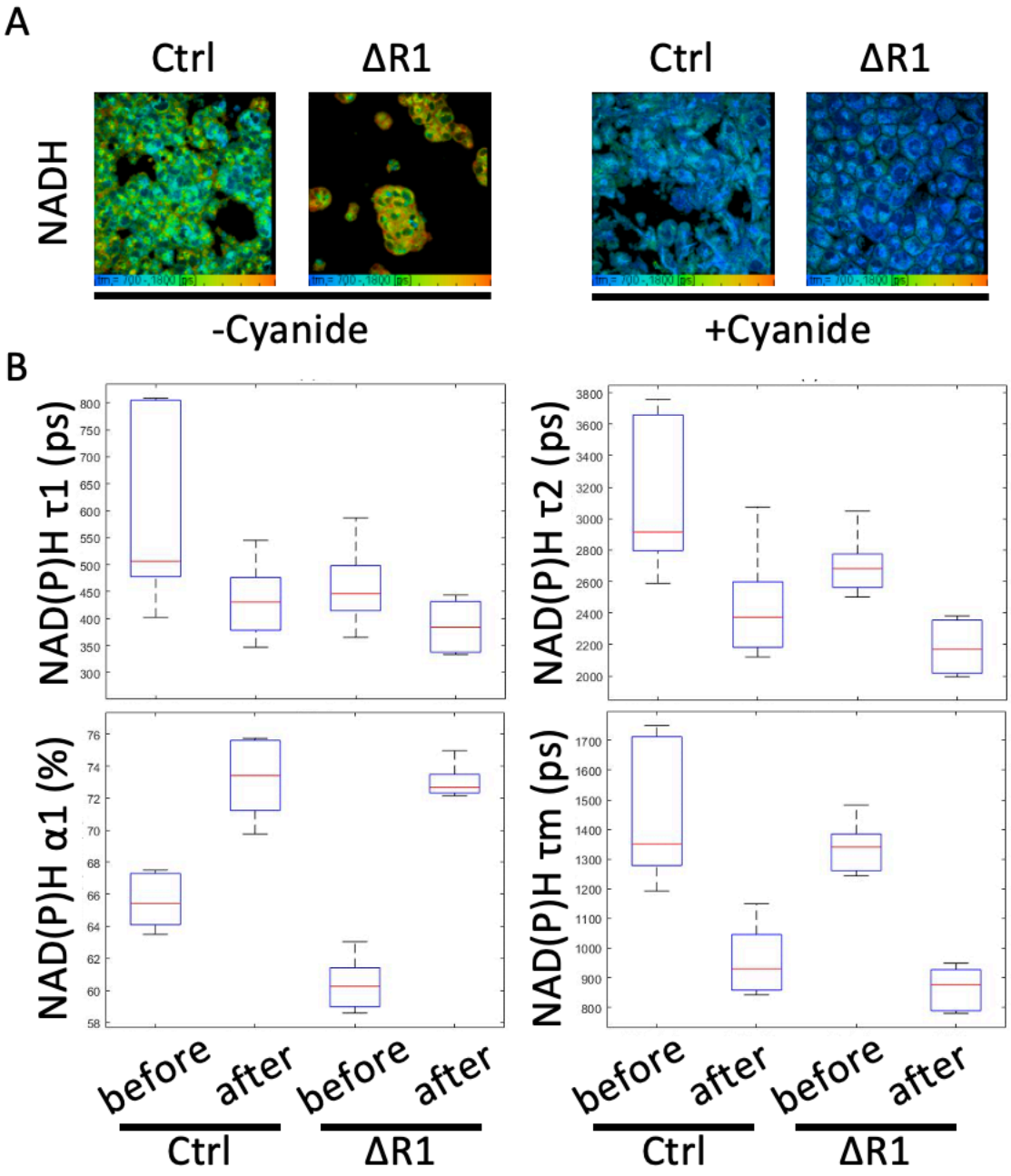

Figure 7 The NADH fluorescence lifetime images measurement in DU145 cells.

A) Representative fluorescence lifetime images of NADH in DU145 cells before and after cyanide treatment; B) fluorescence lifetime parameters including short lifetime (τ_1), long lifetime (τ_2), the proportional component of short lifetime (α_1), and the amplitude-weighted lifetime (τ_m) for NADH. Before (or -Cyanide): control group without cyanide treatment; After (or +Cyanide): with 4 mM cyanide treatment for 5 minutes. Ctrl, $DU145^{Ctrl}$ cells; ΔR1, $DU145^{\Delta R1}$ cells.

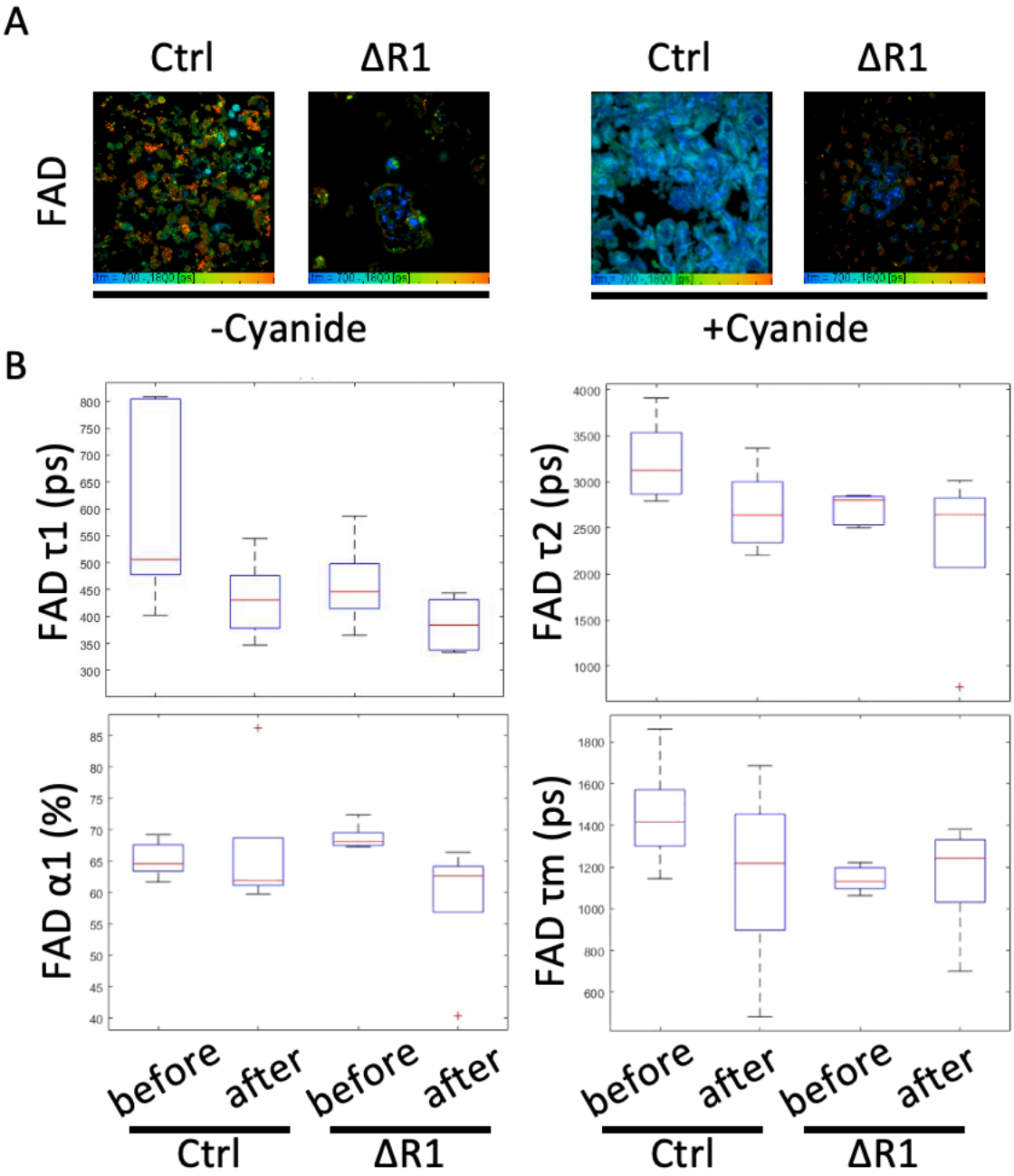

Figure 8 The FAD fluorescence lifetime image measurement in DU145 cells.

A) Representative fluorescence lifetime images of FAD in DU145 cells before and after cyanide treatment; B) fluorescence lifetime parameters including short lifetime (τ_1), long lifetime (τ_2), the proportional component of short lifetime (α_1), and the amplitude-weighted lifetime (τ_m) for FAD. Before (or -Cyanide): control group without cyanide treatment; After (or +Cyanide): with 4 mM cyanide treatment for 5 minutes. Ctrl, $DU145^{Ctrl}$ cells; ΔR1, $DU145^{\Delta R1}$ cells.

Loss of FGFR1 signaling suppresses aerobic glycolysis in PCa cells

To further dissect the role of FGFR1 signaling in metabolic reprogramming in PCa cells, glycolysis was quantified by both OCR and ECAR (extracellular acidification rate) in $DU145^{Ctrl}$ and $DU145^{\Delta R1}$ cells. The Proton Efflux rate (PER) was quantified as an indicator of cellular glycolysis. Decreased glycolysis was observed in $DU145^{\Delta R1}$ cells (**Figure 9A**), with dramatic decreases in basal and compensatory glycolysis (**Figure 9B**). These suggest that $DU145^{\Delta R1}$ cells are more capable of adapting to mitochondrial dysfunction. Meanwhile, we noticed that the post 2-DG acidification was comparable in $DU145^{Ctrl}$ and $DU145^{\Delta R1}$ cells (**Figure 9B**), suggesting that non-glycolytic acidification remained the same. To validate the result, AZD4547 was used to block FGFR1 signaling in DU145 cells prior to glycolysis quantification. A moderately reduced glycolysis rate was observed after a 6-hour treatment (**Figure 10A**), with decreased basal and compensatory glycolysis (**Figure 10B**), suggesting that blocking FGFR1 signaling suppressed glycolysis in DU145 cells.

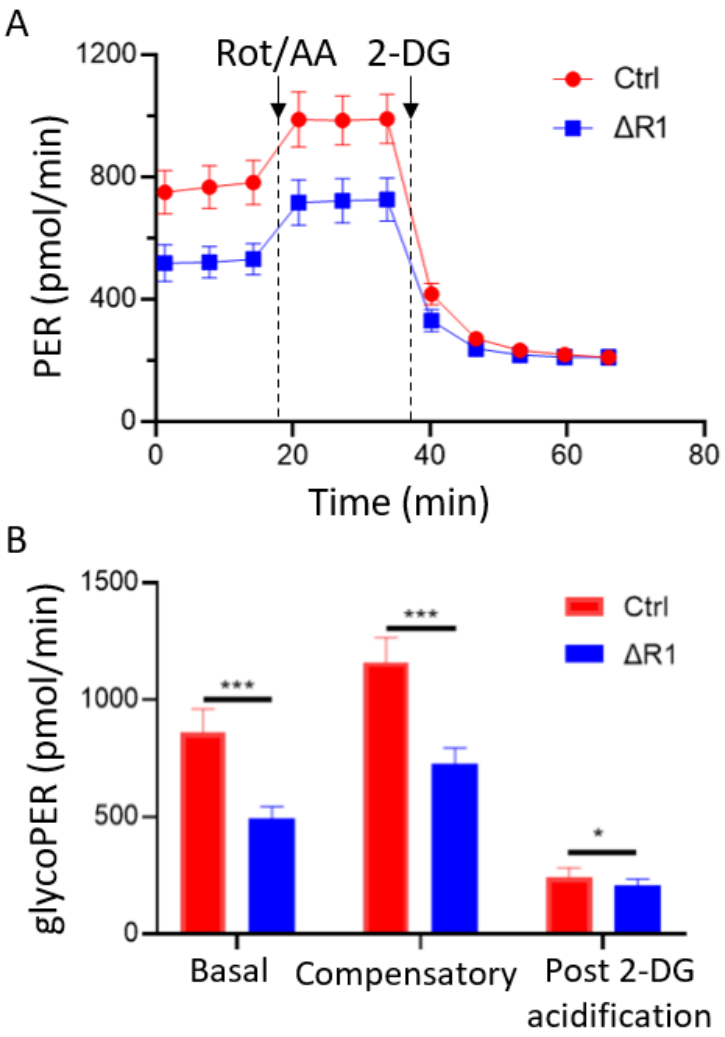

Figure 9 Ablation of FGFR1 suppresses glycolysis in DU145 cells.

A) PER measured in DU145^{Ctrl} (n=21) and DU145$^{\Delta R1}$ cells (n=18) with the addition of Rot/AA and 2-DG; B) Metabolic parameters calculated by OCR and ECAR, including basal glycolysis, compensatory glycolysis, and post 2-DG acidification; Ctrl, DU145^{Ctrl} cells; ΔR1, DU145$^{\Delta R1}$ cells. Error bars represent mean ± SEM. *p<0.05, ***p<0.001.

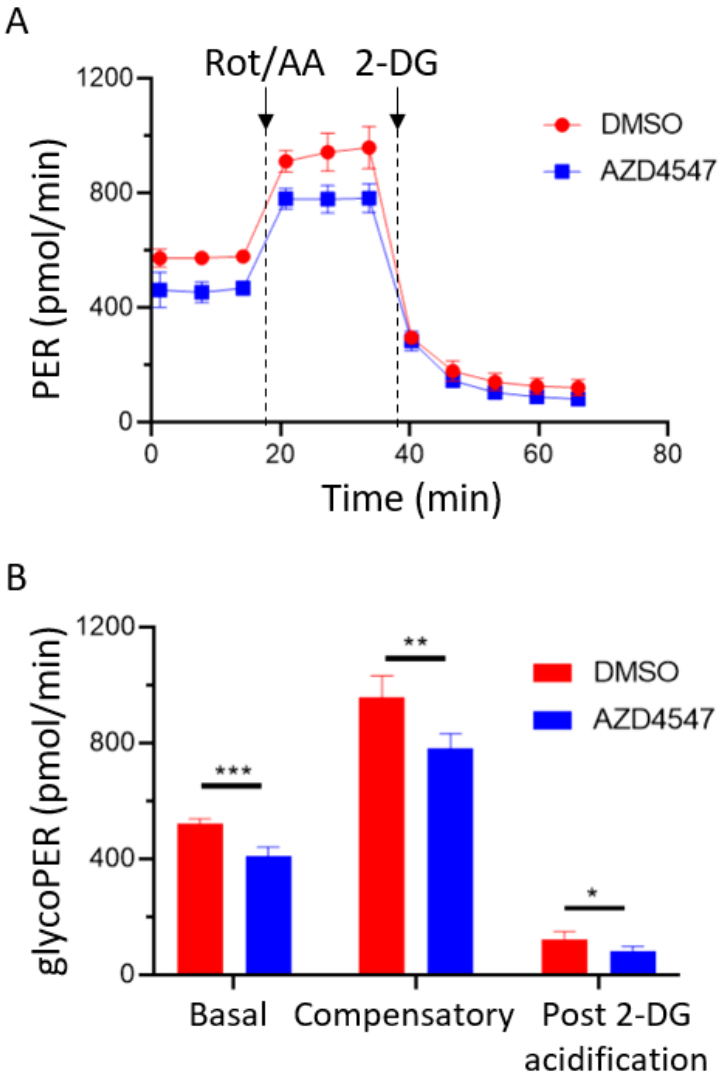

Figure 10 Blocking FGFR1 signaling suppresses glycolysis in DU145 cells.

A) PER measured in DU145 cells in the absence (n=4) or presence (n=5) of AZD4547 with the addition of Rot/AA and 2-DG; B) Metabolic parameters calculated by OCR and ECAR, including basal glycolysis, compensatory glycolysis, and post 2-DG acidification. DMSO, DU145 cells treated with 1% DMSO as the control for 6 hours; AZD and AZD4547, DU145 cells treated with AZD4547 for 6 hours. Error bars represent mean ± SEM. *p<0.05, **p<0.01, ***p<0.001.

Loss of FGFR1 signaling alters ATP production venues

Aerobic glycolysis and mitochondrial respiration are the major metabolic pathways for generating energy to meet the demands of cancer growth, which differs in ATP production efficiency. One of the leading consequences of shifting from aerobic glycolysis to OXPHOS is the alteration of the energy generation map. To determine if ectopic FGFR1 changed the ATP production in PCa cells, ATP produced by mitochondrial respiration (designated mitoATP) and glycolysis (designated glycoATP) was measured separately in DU145 cells. The ratio of mitoATP to glycoATP is shown in **Figure 11** as normalized by total ATP production in the cells. We found that deletion of FGFR1 increased the ratio of mitoATP production from 22% to 27%, and decreased the glycoATP production rate from 78% to 73% (**Figure 11A**). Blocking FGFR1 signaling using AZD4547 led to similar findings, where the mitoATP increased from 33% to 58% and glycoATP dropped from 67% to 42% upon FGFR1 inhibition (**Figure 11B**). These data suggest that FGFR1 deficient DU145 cells rewire their energy generation processes by producing more mitoATP and less glycoATP.

Taken together, these data suggest that ablation of FGFR1 reverses metabolic reprogramming by decreasing aerobic glycolysis and increasing OXPHOS in PCa cells.

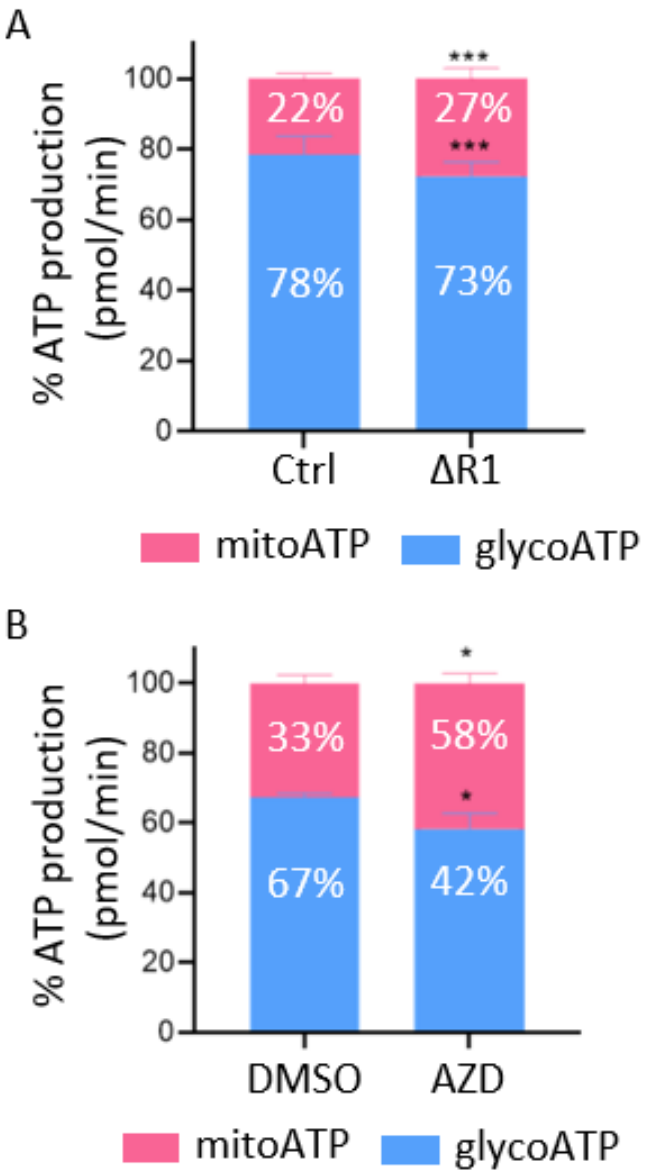

Figure 11 Loss of FGFR1 signaling alters the energy production profiles in DU145 cells.

ATP production from mitochondrial activity and glycolysis were measured in A) $DU145^{Ctrl}$ (n=20) and $DU145^{\Delta R1}$ cells (n=20); and B) DU145 cells in the absence (n=3) or presence (n=3) of AZD4547 with the addition of Oligo and Rot/AA; Ctrl, $DU145^{Ctrl}$ cells; ΔR1, $DU145^{\Delta R1}$ cells; DMSO, DU145 cells treated with 1% DMSO as the control for 6 hours; AZD and AZD4547, DU145 cells treated with AZD4547 for 6 hours. Error bars represent mean ± SEM. *p<0.05, ***p<0.001.

The glucose-dependent pathway is the major target in FGFR1-regulated metabolic reprogramming in PCa cells

The next question to be addressed is how FGFR1 rewires the metabolic network in PCa cells. Apart from glucose-dependent pathways, fatty acid and glutamine may also fuel the TCA cycle (tricarboxylic acid cycle) by β-oxidation and glutaminolysis, respectively, further contributing to the TCA cycle and then OXPHOS [112, 113]. To investigate which metabolic pathway(s) serves as the major target of FGFR1, the Seahorse XF Mito Fuel Flex Test was performed in $DU145^{Ctrl}$ and $DU145^{\Delta R1}$ cells to dissect the dependency and capacity of each metabolite to fuel mitochondrial respiration individually. Multiple inhibitors were used specifically targeting one of these three metabolic candidates: UK5099 as the inhibitor for MPC (mitochondrial pyruvate carrier) was used to block glucose oxidation [114]; BPTES, as the inhibitor for GLS (glutaminase) was used to block glutamine oxidation [115]; and Etomoxir, as the inhibitor for CPT1A (carnitine palmitoyl-transferase 1A) was used to block fatty acid oxidation [116]. The calculation of dependency and capacity was performed according to the equations in the manufacturer's instructions listed below:

Equation 2 Calculation for fuel dependency

$$Fuel\ dependency = \left(\frac{Baseline\ OCR - OCR\ with\ targeted\ inhibitor}{Baseline\ OCR - OCR\ with\ all\ inhibitors}\right) \times 100\%$$

Equation 3 Calculation for fuel capacity

$$Fuel\ capacity = [1 - \left(\frac{Baseline\ OCR - OCR\ with\ other\ 2\ inhibitor}{Baseline\ OCR - OCR\ with\ all\ inhibitors}\right)] \times 100\%$$

The dependency and capacity of each fuel were plotted in **Figure 12**. We found that glucose dependency (accounting for around 55%) is the highest among these three pathways both in $DU145^{Ctrl}$ and $DU145^{\Delta R1}$ cells, while glutamine and fatty acid accounted for 25% and 20% of fuel dependence, respectively (**Figure 12A**, **B** and **C**). This suggests a high reliance on the glucose oxidation pathway to fuel OXHPOS in DU145 cells. An increased glucose dependency representing a higher OCR coming from the glucose-dependent pathway was observed in $DU145^{\Delta R1}$ cells (**Figure 12A**), suggesting the ablation of FGFR1 increased the utilization rate of pyruvate synthesized through glycolysis. The dependency on glutamine and fatty acid pathways remained steady (**Figure 12B** and **C**), suggesting that these two metabolic pathways were not the major target for FGFR1 in regulating metabolic reprogramming in PCa cells. Meanwhile, an increased glucose capacity was observed in $DU145^{\Delta R1}$ cells (**Figure 12D**), suggesting ablation of FGFR1 increased the capability of DU145 cells under certain stress when glutamine and fatty acid pathways were dysfunctional. Reduced glutamine capacity and fatty acid capacity were also observed upon FGFR1 deletion (**Figure 12E** and **F**), suggesting that FGFR1 was not the major regulator for these two metabolic pathways.

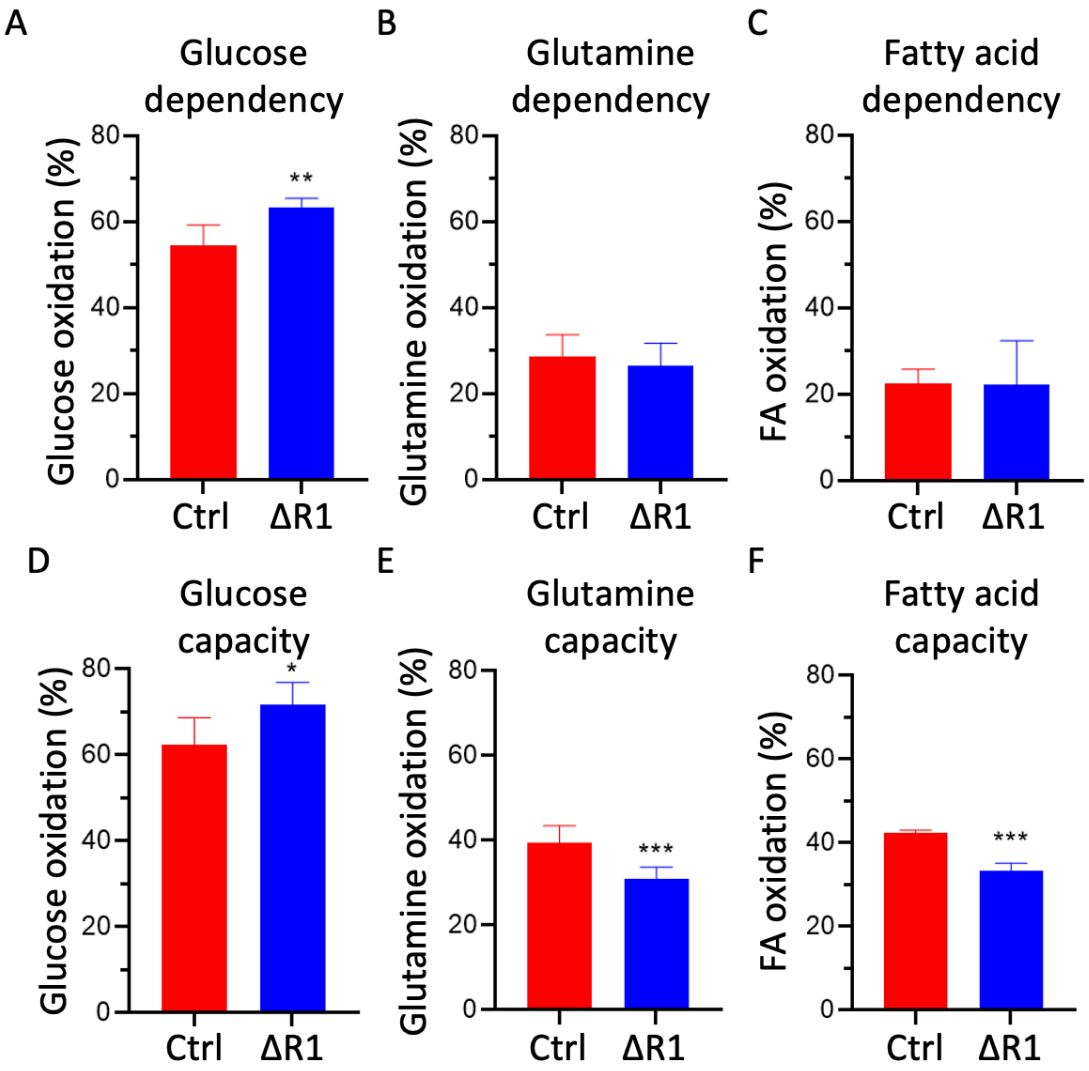

Figure 12 Dependency and capacity of three metabolic pathways in DU145 cells.

Fuel dependency of A) glucose; B) glutamine; and C) fatty acid and fuel capacity of D) glucose; E) glutamine; and F) fatty acid in $DU145^{Ctrl}$ (n=6) and $DU145^{\Delta R1}$ cells (n=6) were calculated. Ctrl, $DU145^{Ctrl}$ cells; ΔR1, $DU145^{\Delta R1}$ cells; Error bars represent mean ± SEM. *p<0.05, **p<0.01, ***p<0.001.

MPC1 and PDHc are potential downstream targets of FGFR1

To determine the mechanism of how ectopic FGFR1 suppressed metabolic reprogramming in PCa cells, RNA-seq was performed using a NextSeq^{TM} 550 system (Illumina, CA) for potential downstream screening. The reads were transformed to FPKM (paired fragments per kilobase of transcript per million mapped reads) and mapped as TopHat and Cufflinks as previously described [83-87]. DEGs (Differentially expressed genes) were defined in DU145^{Ctrl} and DU145$^{\Delta R1}$ cells by fold change ≥ 2 and FDR < 0.05 and plotted in volcano plot and heatmap using R scripts. A total of 1620 DEGs were identified, with 717 genes upregulated and 903 genes downregulated (**Figure 13**). To precisely look at the groups of interest, genes related to OXPHOS and glycolysis were selected and plotted to generate DEGs of interest (**Figure 14A**). The heatmap that shows those DEGs individually is presented in **Figure 14B**. We noticed two genes involved in OXPHOS whose expression was significantly increased in DU145$^{\Delta R1}$ cells, suggesting that they were potential downstream targets of FGFR1 signaling. 1) MPC1 (Mitochondrial Pyruvate Carrier 1), a key component of pyruvate transporter responsible for pumping pyruvate into mitochondria. It serves as the major supply of pyruvate as metabolic fuel to the TCA cycle and plays a critical role in maintaining the homeostasis between glycolysis and OXPHOS [117]. 2) PDP1 (Pyruvate dehydrogenase phosphatase), a key regulator of PDHc (pyruvate dehydrogenase complex) activity. It facilitates the pyruvate oxidation towards acetyl-CoA through activating PDHc [118, 119].

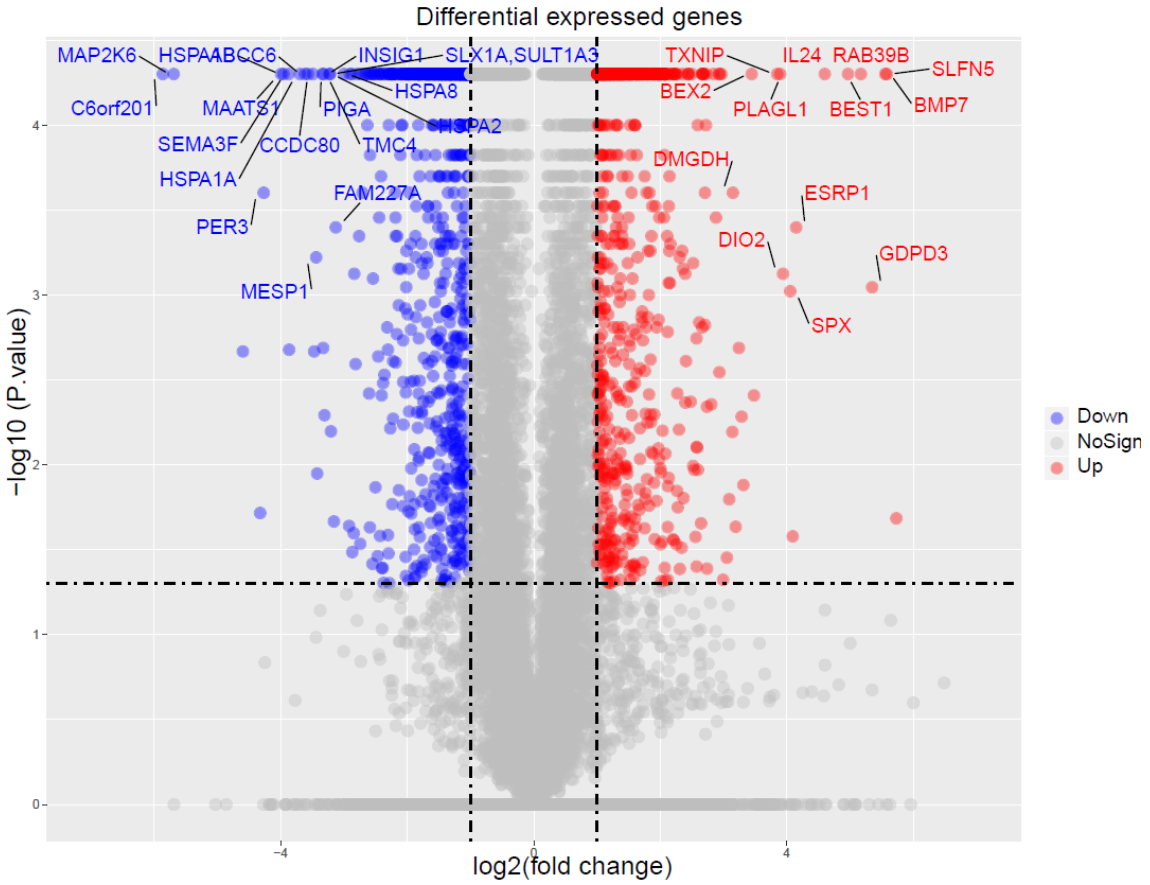

Figure 13 DEGs in response to FGFR1 ablation in DU145 cells.

Volcano plot of DEGs downregulated (blue) and upregulated in DU145$^{\Delta R1}$ cells. DEGs plotted were selected with fold change ≥ 2 and FDR < 0.05; DEGs labeled with names were selected with fold change ≥ 8 and FDR < 0.0001.

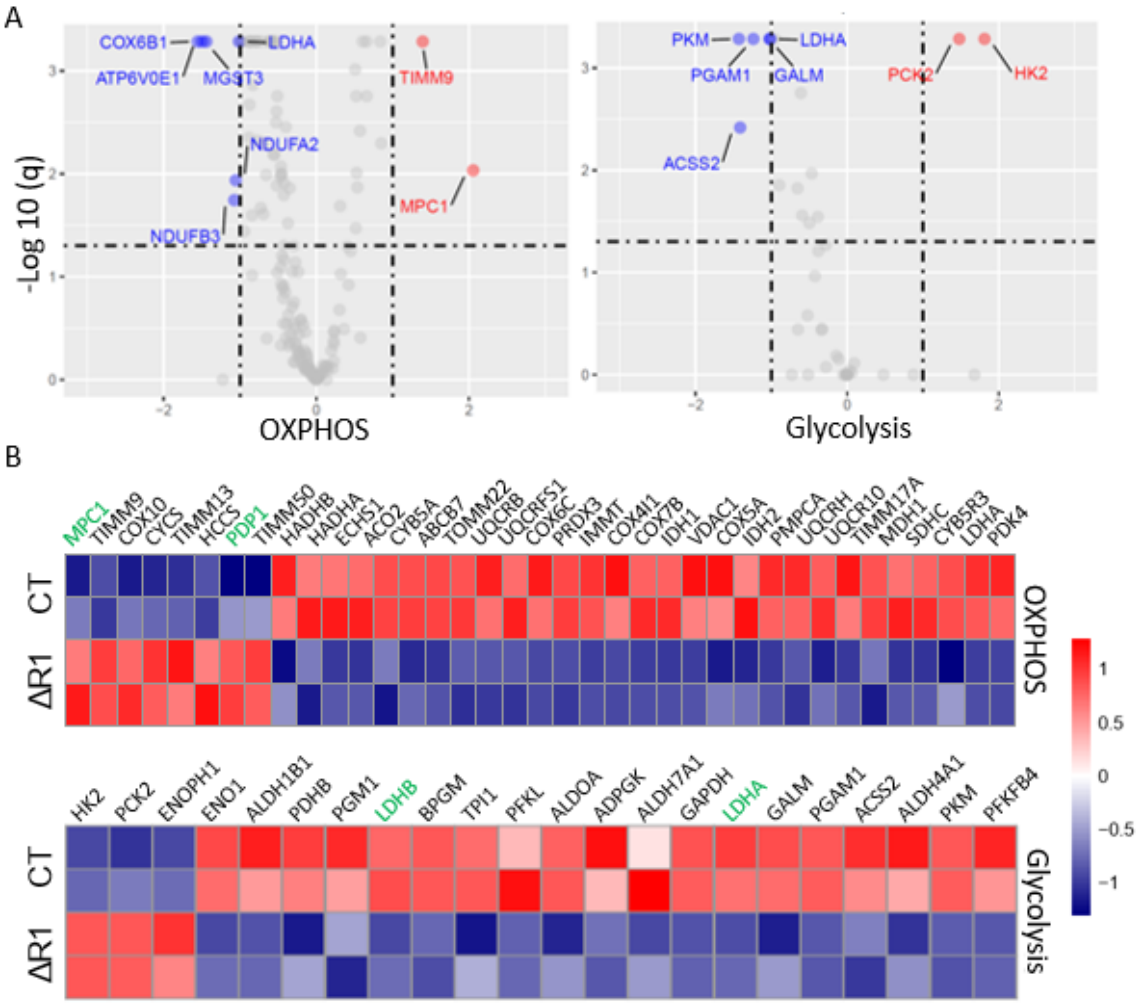

Figure 14 DEGs involved in OXPHOS and aerobic glycolysis pathways.

A) Volcano plot and B) Heatmap of DEGs from transcripts of DU145^{Ctrl} and DU145$^{\Delta R1}$ cells, as green indicates key genes involve in OXPHOS and glycolysis pathway. Ctrl, DU145^{Ctrl} cells; ΔR1, DU145$^{\Delta R1}$ cells.

Taken together, ablation of FGFR1 increased OXPHOS and decreased aerobic glycolysis leading to metabolic reprogramming in DU145 cells, which mainly relied on the glucose-dependent pathway. The underlying mechanism of how FGFR1 promotes metabolic reprogramming remains to be determined. Our data suggested that MPC1 and PDP1 were the two potential downstream targets responsible for FGFR1 to regulate cell metabolism at the mRNA level. More efforts are critically needed to demonstrate the linkage between PDP1, MPC1, and FGFR1.

Ablation of FGFR1 ameliorates the immunosuppressive of the TME in PCa

It is by far unclear the factors that cause cancer cells to rewire their metabolism, although it has been proposed to be a response to the stress from nutrition and oxygen scarcity [70]. However, the reprogrammed cell metabolism contributes to establishing a TME that favors tumor growth and immune evasion [71, 72]. Recent reports showed that tumor-derived lactate exhibits suppressive effects on T cell proliferation and activation, leading to immunosuppression [73-75]. Therefore, selectively reducing lactate accumulation via suppressing glycolysis in cancer cells is a potential strategy to ameliorate the "cold" microenvironment in PCa [120, 121]. However, immune cell function and growth also require aerobic glycolysis and OXPHOS. Suppression of aerobic glycolysis induced $CD4^+$ T cell apoptosis and promoted differentiation towards Treg [122]. In addition, $CD8^+$ T cells primarily use aerobic glycolysis during the effector phase [123, 124]. Together, it makes it counterproductive to treat patients with metabolic inhibitors to decrease lactate accumulation. We found that ablation of FGFR1 reverses metabolic reprogramming in cancer cells, leading to lower tumor-derived lactate

accumulation in the TME [76]. These findings reveal the possibility of blocking FGFR1 as an alternative way to specifically decrease tumor-derived lactate to subvert immunosuppression in PCa.

To validate that T cells did not express FGFR1, real-time PCR was used to quantitate mRNA expression of *Fgfr1* in T cells and B cells isolated from mouse splenocytes through Fluorescence-activated cell sorting (FACS) enrichment. No mRNA expression of *Fgfr1* was observed in isolated mouse T and B cells (**Figure 15A**). To understand whether FGFR1 inhibitor treatment disrupted aerobic glycolysis in T cells, lactate production in the absence or presence of AZD4547 was measured in isolated T cells. The data showed no significant difference in lactate production between the two groups (**Figure 15B**). Together, the finding suggested that FGFR inhibition had the potential to specifically suppress lactate production in PCa without disturbing aerobic glycolysis in T cells.

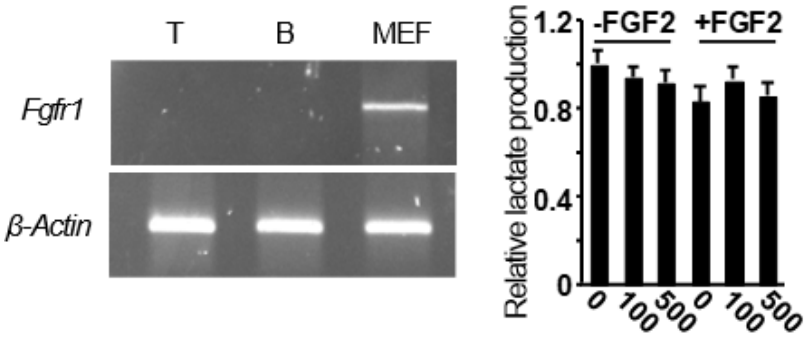

Figure 15 FGFR1 is not expressed in mouse T cells purified from splenocytes.
A) Real-time RT-PCR analysis of *Fgfr1* expression; B) Lactate production of T cells in the absence or presence of AZD4547. T: purified T cells; B: purified B cells; MEF: mouse embryonic fibroblasts. Error bars represent mean ± SEM.

To gain further insight into how the loss of FGFR1 signaling changed the immune profile in the TME, RNA-seq was performed to compare gene expression profiles in $DU145^{Ctrl}$ and $DU145^{\Delta R1}$ cells as described previously. Based on GO analyses, the genes encoding cytokines and chemokines were selected for functional analysis. We found most of the DEGs of interest were involved in the activation and proliferation of immune cells. A total of 13 genes were involved in the positive regulation of T cell-based immunity (**Figure 16A**). To gain a better understanding of these DEGs of interest, a heatmap displaying these DEGs individually was generated by R script. We observed increased expression of cytokines previously reported to positively contribute to T cell function: IL-24 [125], IL-11 [126], IL-12A [127], and IL-18 [128]; as well as decreased expression of CD276 (also called B7-H3) [129], an immune checkpoint molecule. These data suggest that ablation of FGFR1 increased pro-immune cytokines, and decreased immunosuppressive molecules secreted by cancer cells, and therefore, promoted T cell-based immunity.

Taken together, we hypothesize that blocking FGFR1 signaling specifically in cancer cells will reduce the immunosuppressives of the TME, and thus increase the efficacy of PCa immunotherapy.

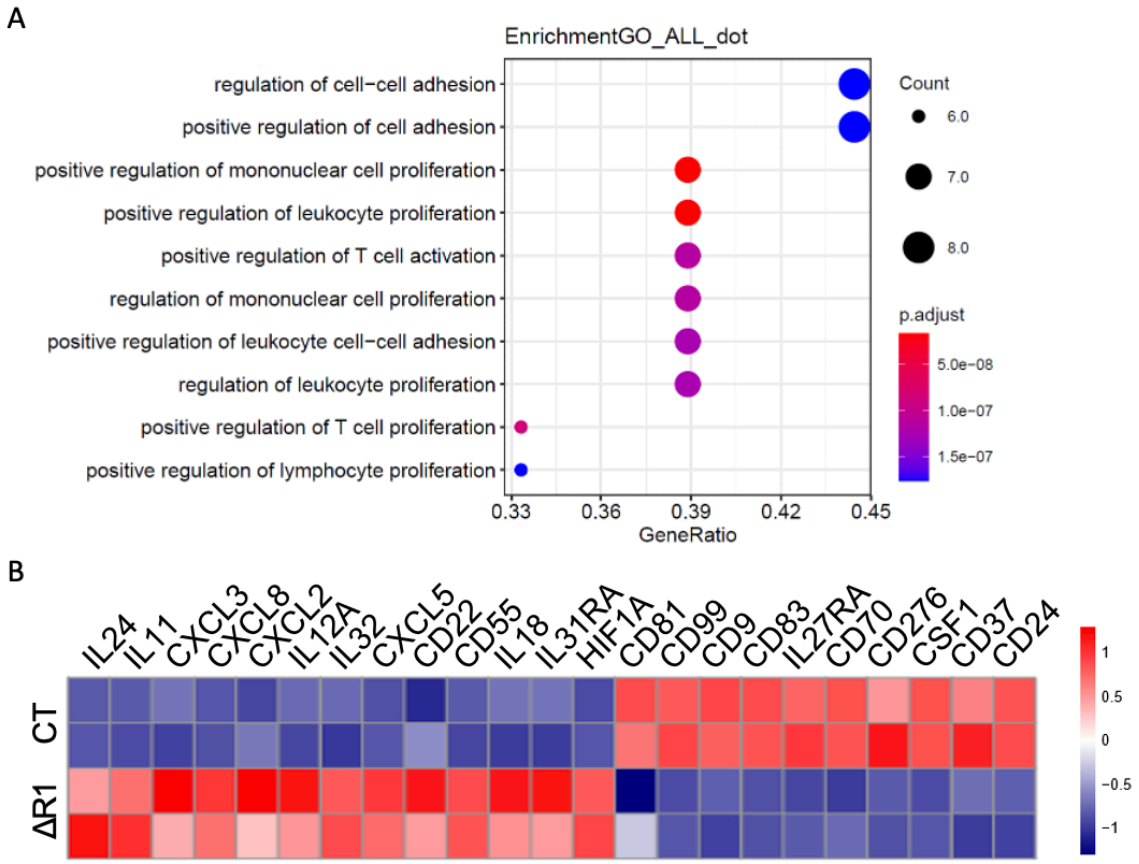

Figure 16 Ablation of FGFR1 alters cytokine profile.

A) Functional enrichment analysis based on GO terms, and only significant terms are displayed; B) Heatmap of DEGs from transcripts of $DU145^{Ctrl}$ and $DU145^{\Delta R1}$ cells. Ctrl, $DU145^{Ctrl}$ cells; ΔR1, $DU145^{\Delta R1}$ cells.

DU145 conditioned medium suppresses T cell growth

To investigate how FGFR1 signaling in PCa cells affected T cell function, Jurkat cells were cultured with 10% of (1) control medium, (2) conditioned medium from DU145 cells, or (3) conditioned medium from $DU145^{\Delta R1}$ cells for 5 days. Each group was treated with increasing concentrations of exogenous lactic acid to evaluate the effect of accumulating lactate in TME on T cell proliferation (**Figure 17A**). The relative cell viability was estimated by OD_{450} value following the CCK8 assay manufacturer's instructions, normalized by day 0 (4 hours after cell seeding), and mapped by heatmap (**Figure 17B**). We found decreased cell viability in Jurkat cells cultured in $DU145^{Ctrl}$ conditioned medium compared to the controlled medium and those cultured in the $DU145^{\Delta R1}$ conditioned medium on day 3 and day 4. The relative cell viability in each group on day 4 and the growth inhibition rate under 10 mM lactate acid calculated by the equation listed below were selected to plot with the lactate concentration.

Equation 4 Calculation for relative cell viability

$$Relative\ cell\ viability = \left(\frac{OD}{OD\ without\ lactate\ acid\ in\ control\ group}\right) \times\ 100\%$$

As expected, the higher lactate acid concentration in the medium resulted in the more severe suppression of Jurkat cell viability (**Figure 17C**). No Jurkat cell survived on day four after being treated with 30 mM lactate acid. In addition, treated with $DU145^{Ctrl}$ conditioned medium decreased Jurkat responsiveness to the increased lactate concentration in the culture medium. A similar effect was not found in the group treated

with DU145$^{\Delta R1}$ conditioned medium (**Figure 17C**). Together, these data suggest that ablation of FGFR1 signaling blunts the activity of DU145 cells to suppress the growth and survival of Jurkat cells.

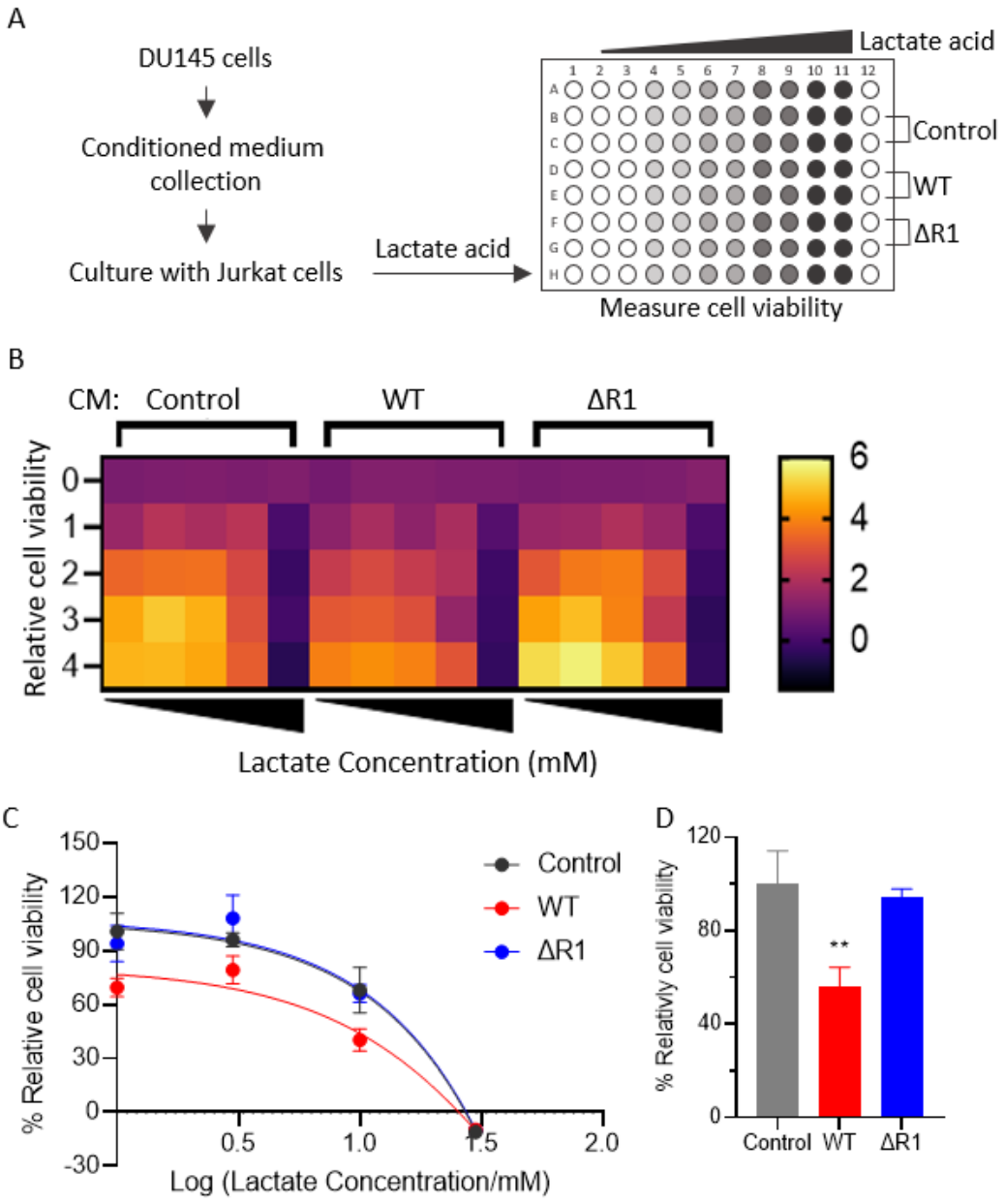

Figure 17 DU145 conditional medium suppressed the cell growth of Jurkat cell.

A) Experiment scheme for conditioned medium collection and lactate acid addition; B) Heatmap for Jurkat cell growth in the indicated conditioned medium with or without lactic acid; C) Curve plot for relative cell viability changed on day 4, and data were all normalized by the control group (complete medium) without lactate acid addition; D) Growth inhibition rate. CM: conditioned medium; Complete: complete medium; CT: $DU145^{Ctrl}$ cells conditioned medium; ΔR1, $DU145^{\Delta R1}$ cells conditioned medium. Error bars represent mean ± SEM. *p<0.05.

Ablation of Fgfr1 increased tumor-infiltrating T cells in TRAMP tumors

To investigate whether ectopic FGFR1 in PCa cells contributed to an immunosuppressive TME, TRAMP (Transgenic adenocarcinoma of the mouse prostate) mice bearing epithelial-specifically ablation of *Fgfr1* ($TRAMP^{\Delta R1}$) were generated through crossing TRAMP mice, ARR_2PBi-*Cre* mice, and $Fgfr1^{loxP/loxP}$ mice as described previously [55]. The PCa tissues were harvested from the mice at the age of 28-32 weeks old. FACS and RT-PCR analyses were used to identify the population of $CD8^+$ T cells. We found that in mice lacking prostate epithelial FGFR1, the tumor size was smaller with a significant increase in $CD3^+CD8^+$ T cells than in control mice (**Figure 18A** and **B**). Quantitative RT-PCR analyses showed a considerable decrease of *Fgfr1* expression in $TRAMP^{\Delta R1}$ tumor. The results also showed that the CD8 mRNA abundance was lower in $TRAMP^{\Delta R1}$ tumor compared with the controlled TRAMP tumor (**Figure 18C**). Taken together, these data suggest that ablation of *Fgfr1* increased tumor-infiltrating T cell population, and therefore, promoted the immune response in TRAMP mice.

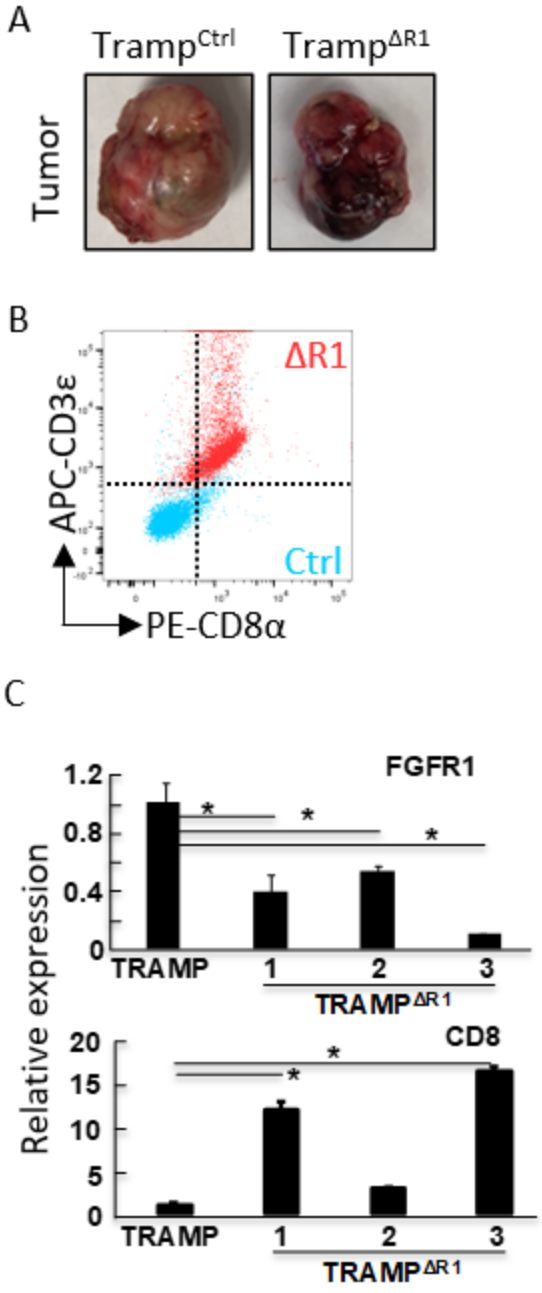

Figure 18 Ablation of *Fgfr1* increased tumor-infiltrating T cell in TRAMP mice

A) Representative images for tumors collected from TRAMP^{Ctrl} and TRAMP$^{\Delta R1}$ mice; B) Dot plot represents the distribution of CD3^{+}CD8^{+} T cells, blue dots indicate the tumor-infiltrating lymphocytes from TRAMP^{Ctrl} tumor while red dots indicate those from TRAMP$^{\Delta R1}$ mice. C) RT-PCR analysis of *Fgfr1* and *CD8* in tumor tissues. Error bars represent mean ± SEM. *p<0.05.

Ablation of Fgfr1 increased efficacy of anti-PD-1 antibody treatment in the TRAMP model

As one of the inhibitory checkpoint pathways inhibiting T cell-mediated immune responses, programmed cell death receptor-1 (PD-1) and its ligand programmed cell death ligand-1 (PD-L1) has been put at the center of immune checkpoint studies [130]. To date, the clinical development of monotherapy targeting PD-1 and PD-L1 for PCa has been unsuccessful, partly due to the unfavorable survival of immune cells in the TME [131]. Combination therapies started to gather momentum in the past decade, which aim to increase the potential of targeting PD-1 and PD-L1 checkpoint treatment for PCa [132].

To determine whether ablation of *Fgfr1* increased the efficacy of anti-checkpoint therapy, a 14-day treatment of monoclonal anti-PD-1 antibody (BioXcell, #BE0146) was performed by intraperitoneal injection every two days at 200 mg/dose in $TRAMP^{Ctrl}$ and $TRAMP^{\Delta R1}$ mice. To precisely define the time to start the treatment, spontaneous tumor growth of the mice was monitored by ultrasound imaging biweekly starting at the age of 26- 28 weeks old following the protocol described previously [94, 95]. The first injection was given when the tumor size reached around 1 mm^3 measured by ultrasound imaging. Tumor volume after therapy was calculated using tumor width and length as previously described [96]. The results showed that tumor size shrank with anti-PD-1 antibody in $TRAMP^{\Delta R1}$ mice compared to $TRAMP^{Ctrl}$ mice(**Figure 19**). To validate the knockout efficiency of Fgfr1 in $TRAMP^{\Delta R1}$ mice, IF (immunofluorescence) staining was performed on tumor tissue sections from $TRAMP^{Ctrl}$ and $TRAMP^{\Delta R1}$ mice. As expected,

the expression level of Fgfr1 was significantly decreased in TRAMP$^{\Delta R1}$ compared to TRAMP^{Ctrl} mice (**Figure 20**). To gain further understanding of whether ablation of *Fgfr1* promotes an immune response in TRAMP mice, IF staining was performed on tumor tissue with anti-CD8α antibody. A dramatic increase in CD8^{+} tumor-infiltrating T cells was observed in TRAMP$^{\Delta R1}$ mice treated with anti-PD-1 antibody (**Figure 21** and **22**), suggesting that ablation of *Fgfr1* improved the efficacy of anti-PD-1 antibody in TRAMP mice.

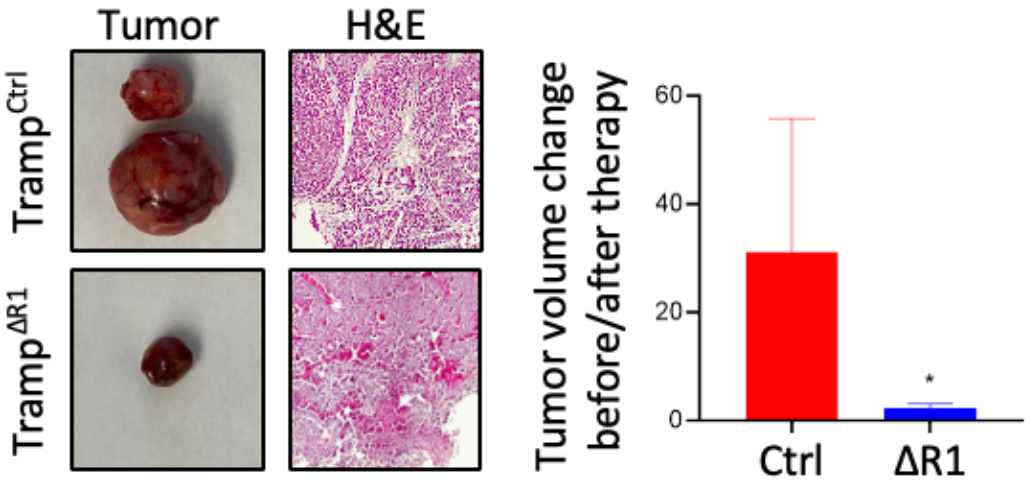

Figure 19 Tumor size shrank after anti-PD-1 antibody therapy in TRAMP$^{\Delta R1}$ mice. Representative images for tumor tissues and H&E staining for TRAMP^{Ctrl} and TRAMP$^{\Delta R1}$ mice. The tumor volume change before and after therapy were plotted. Ctrl: TRAMP^{Ctrl} mice with anti-PD-1 treatment; ΔR1: TRAMP$^{\Delta R1}$ mice with anti-PD-1 treatment. Error bars represent mean ± SEM. *$p<0.05$.

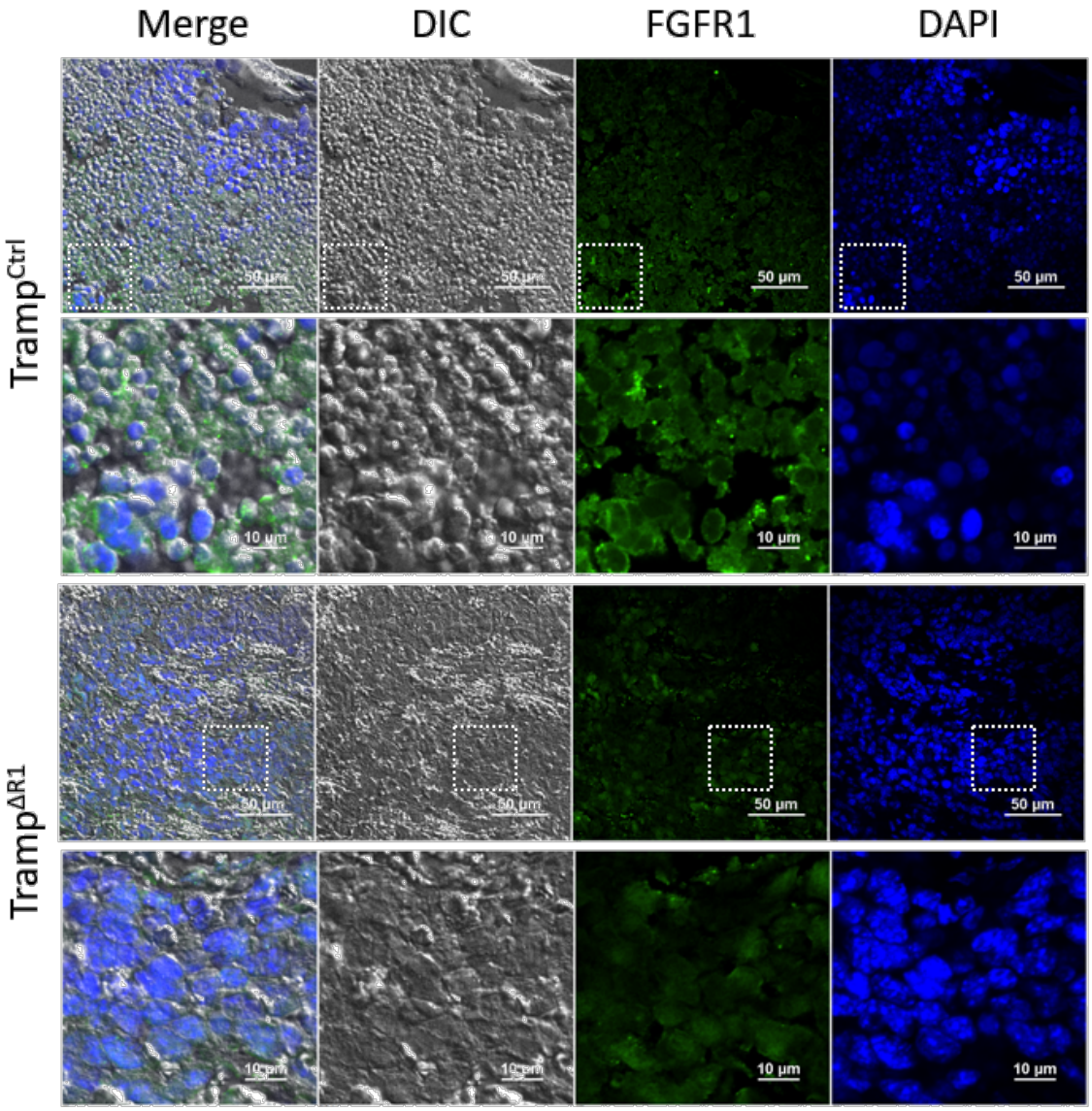

Figure 20 Validation of *Fgfr1* knockout efficiency in TRAMP$^{\Delta R1}$ mice.

Representative images of IF staining from TRAMP^{Ctrl} and TRAMP$^{\Delta R1}$ mice. Tissue sections were immunostained with anti-Fgfr1. The nucleus was counterstained with DAPI. The zoom field (at the bottom) is labeled by a white square with the dotted line.

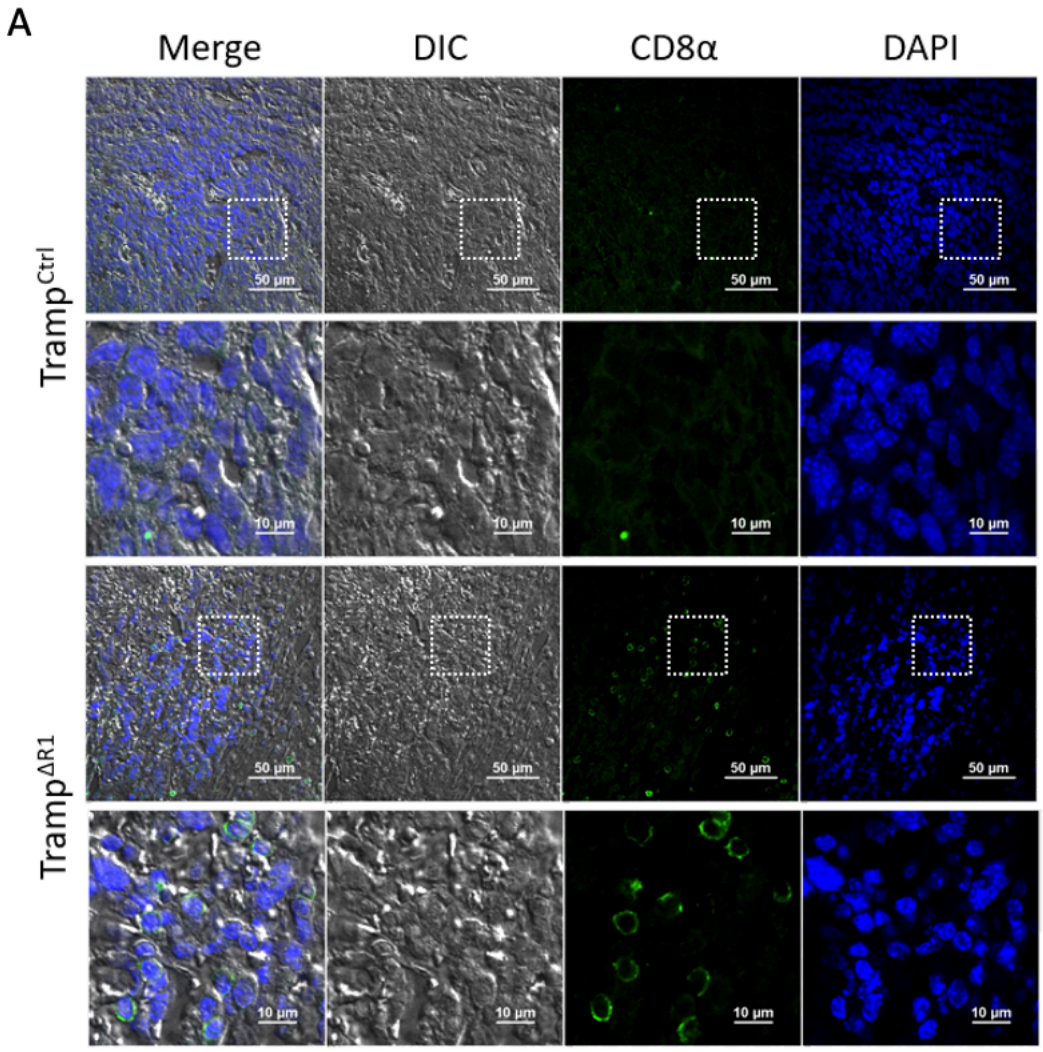

Figure 21 Ablation of *Fgfr1* increases CD8$^+$ tumor-infiltrating T cells in TRAMP$^{\Delta R1}$ mice treated with anti-PD-1 antibody.

Representative images of IF staining from TRAMP^{Ctrl} and TRAMP$^{\Delta R1}$ mice. Tissue sections were immunostained with anti-CD8α. Nuclei were counterstained with DAPI. The zoom field (at the bottom) is labeled by a white square with the dotted line.

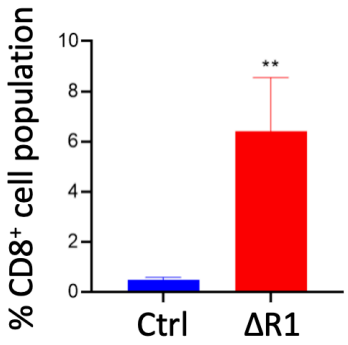

Figure 22 *Fgfr1* knockout leads to increased CD8$^+$ tumor-infiltrating T cells in TRAMP mice treated with anti-PD-1 antibody.

Quantification of CD8$^+$ tumor-infiltrating T cells in TRAMP^{Ctrl} and TRAMP$^{\Delta R1}$ mice receiving anti-PD-1 antibody treatment. Ctrl: TRAMP^{Ctrl} mice with anti-PD-1 treatment; ΔR1: TRAMP$^{\Delta R1}$ mice with anti-PD-1 treatment. Error bars represent mean ± SEM. **p<0.001.

The combination of AZD4547 and anti-PD-1 antibody treatment effectively increases the CD8$^+$ T cell-mediated immune response and suppresses tumor growth

To further determine whether FGFR1 could serve as a potential target for improving anti-checkpoint therapy in the clinic, the efficacy of combination therapy using AZD4547, a specific FGFR1 inhibitor functioning in an ATP-competitive manner [107] and anti-PD-1 antibody, was evaluated in the TRAMP mouse model. TRAMP mice were randomly divided into four groups designated as Control, AZD4547 single-agent, anti-PD-1 single-agent, and AZD4547 + anti-PD-1 combination therapy, respectively. Animals in the control and AZD4547 groups received InVivoMAb rat IgG2a isotype control in the absence or presence of AZD4547 at 5 mg/kg body weight, while mice in the anti-PD-1 and combination groups received monoclonal antibody anti-PD-1 intraperitoneal injection every two days at 200 mg/dose following the

administration scheme indicated in Chapter II. The first injection was given when the prostate tumor size reached around 1 mm^3 measured by ultrasound.

No significant difference was observed in single-agent treatments either using AZD4547 or anti-PD-1 antibody. The result showed that tumor size significantly decreased in TRAMP mice with combination therapy compared to control and single-agent treatments (**Figure 23A** and **B**), indicating that inhibition of Fgfr1 together with anti-checkpoint inhibition suppressed tumor growth effectively. T cell infiltration was quantified by CD8α staining in the tumor tissues. We observed an increased population of $CD8^+$ tumor-infiltrating T cells in the combination therapy group (**Figure 24** and **25**). To further validate the result, FACS analysis was performed to quantify the infiltrating T cells in TRAMP mouse tumors. We found that the number of $CD3^+CD8^+$ tumor-infiltrating T cells was significantly increased in the combination group (**Figure 26**). To validate the result, we took advantage of Imaging mass cytometry (IMC) technology to further dissect the different immune cell populations upon combination therapy. The segmentation was performed using a published workflow as described in Chapter II (**Figure 27A**) [98, 99]. R scripts were used to generate tSNE plots, and a total of 6 populations were identified using the classic cell marker described in Chapter II (**Figure 27B**). The result showed an increased abundance of $CD8^+$ T cells, dendritic cells, and MDSCs, while the macrophage population was significantly reduced in the combination group (**Figure 27C**).

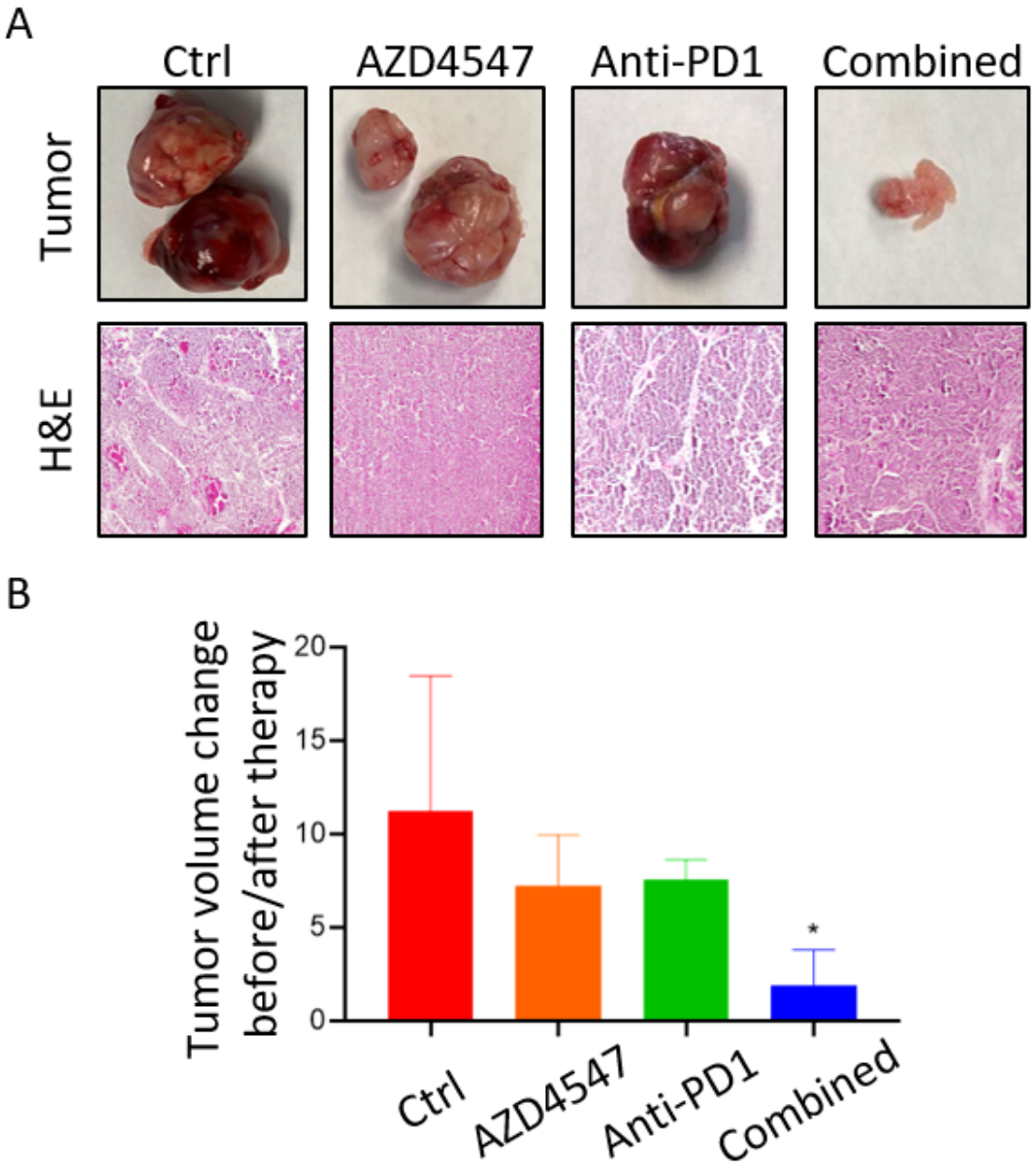

Figure 23 Combination of AZD4547 and anti-PD-1 decreased tumor volume in TRAMP mice.

A) Representative images for PCa tissues and H&E staining of TRAMP mice following single- or combination treatment with AZD4547 and anti-PD-1 antibody. The tumor volume changes before and after therapy were plotted. N = 2 mice/group. PBS: TRAMP with IgG2a as control; AZD4547: TRAMP with AZD4547 and IgG2a treatment; Anti-PD1: TRAMP with anti-PD-1 antibody treatment; Combined: TRAMP with AZD4547 and anti-PD-1 antibody combination treatment. Error bars represent mean ± SEM. *$p<0.05$.

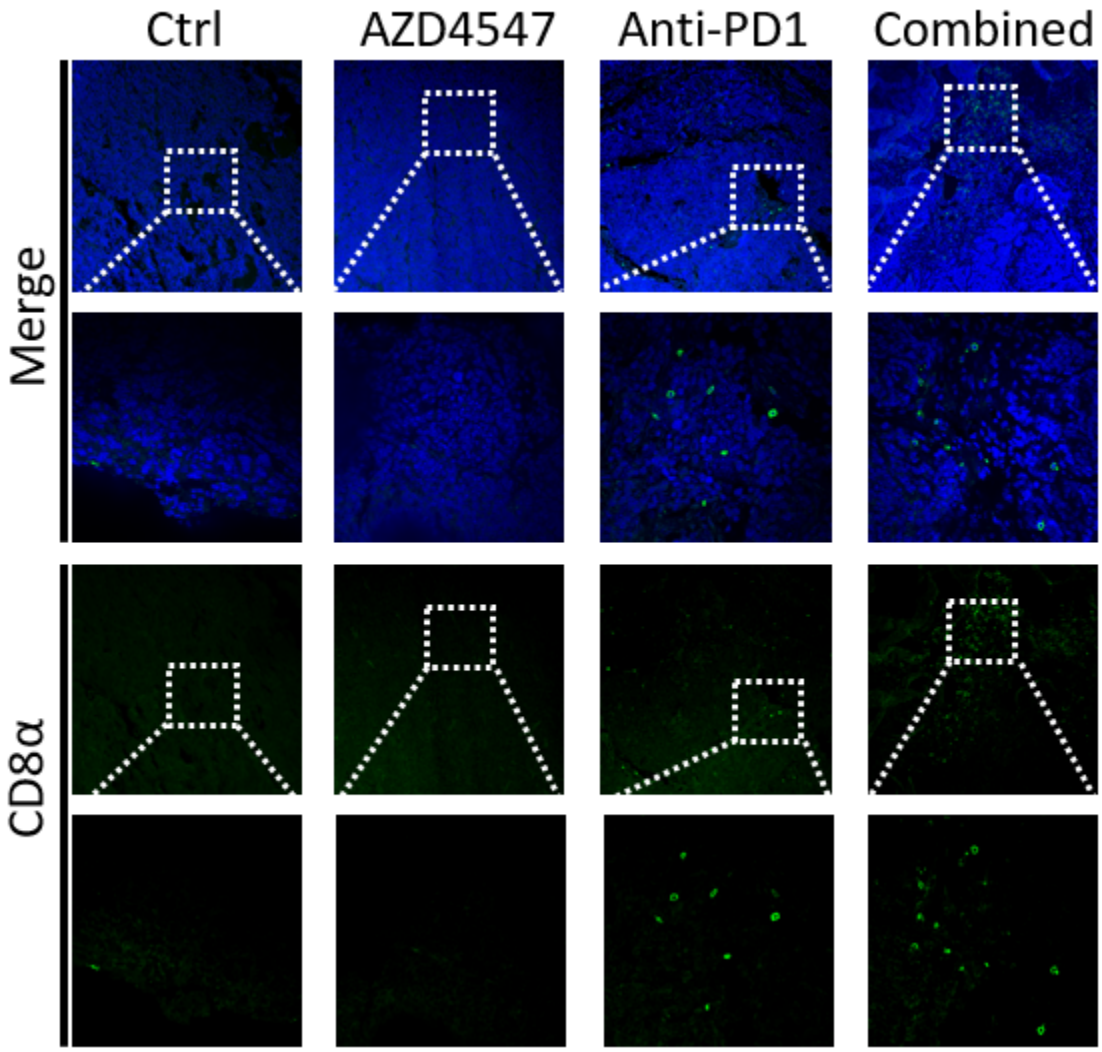

Figure 24 Combination therapy increase CD8$^+$ T cells in TRAMP mice.

Representative images for IF staining from TRAMP mice receiving control (Ctrl), single-agent (AZD4547 or anti-PD1, respectively), and combination (combined) therapy. Tissue sections were stained with anti-CD8α. The nucleus was counterstained with DAPI. The zoom field (in the bottom) is labeled by a white square with the dotted line.

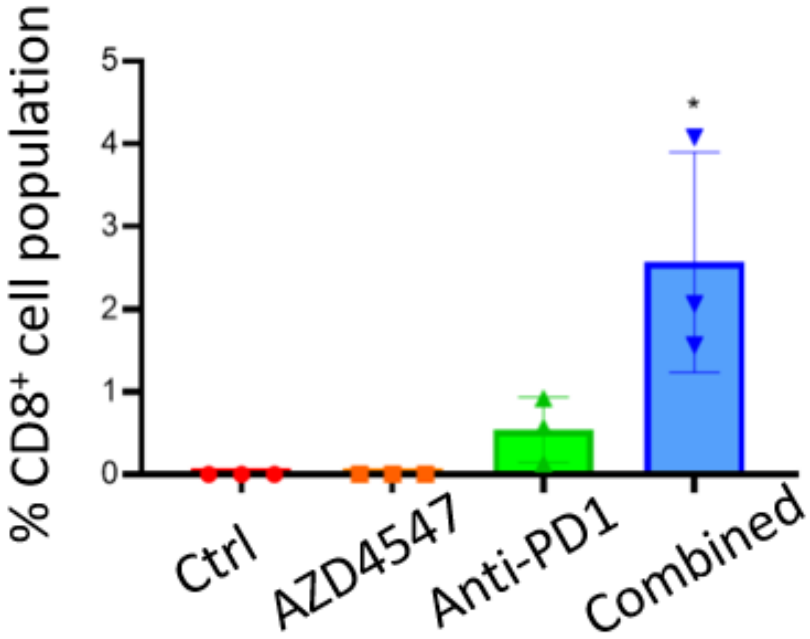

Figure 25 Combination of AZD4547 and anti-PD-1 antibody increased $CD8^+$ tumor-infiltrating T cells in TRAMP mice.

Quantification of $CD8^+$ tumor-infiltrating T cells from TRAMP mice receiving control (Ctrl), single-agent (AZD4547, and anti-PD1, respectively), and combination (combined) therapy. Error bars represent mean ± SEM. **$p<0.001$.

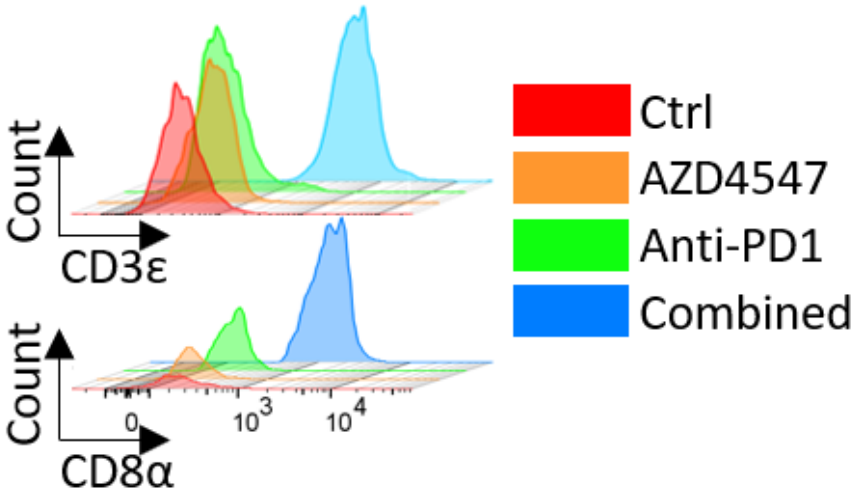

Figure 26 Combination treatment of AZD4547 and anti-PD-1 antibody increased $CD3^+$ $CD8^+$ tumor-infiltrating T cells in TRAMP mice.

The histogram plot represents the distribution of $CD3^+CD8\alpha^+$ T cells from TRAMP mice receiving control (Ctrl, red), single-agent (AZD4547, orange; anti-PD1, green), and combination (combined, blue) therapy.

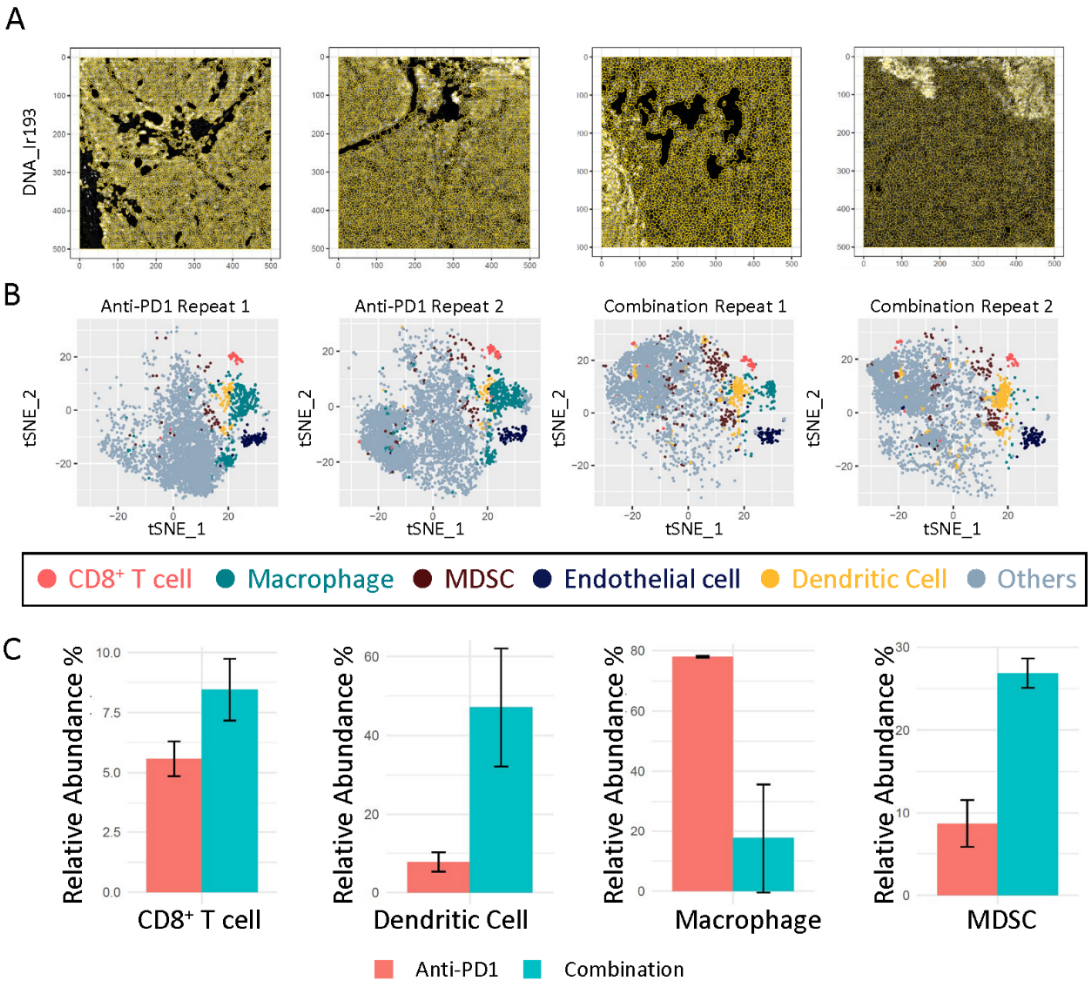

Figure 27 Combination therapy altered TIL subpopulations in PCa.

A) Cell segmentation of the sections used for IMC analysis; B) tSNE plots of mouse samples colored by identified cell types; C) The relative abundance of 4 types of immune cells in total tumor-infiltrating lymphocytes. Yellow line: cell border; white dot: DNA. Error bars represent mean ± SEM.

Taken together, these data suggest that a combination of AZD4547 and anti-PD-1 antibody effectively increases the $CD8^+$ T cell-mediated immune response and suppresses tumor growth in the TRAMP model and therefore, reveals the potential of using FGFR1 inhibitors as a novel combination anti-checkpoint strategy for PCa treatment.

High FGFR1 expressing epithelial cells is negatively correlated to T cell infiltration in PCa patients

To further investigate whether ectopic FGFR1 is associated with the "cold" TME in human PCa, we analyzed the public scRNA-seq database to determine whether FGFR1 expression was correlated with T cell infiltration profiles in PCa patient samples. The scRNA-seq data that were acquired from patients diagnosed with localized PCa as previously described [103] was downloaded from NCBI's GEO (Gene Expression Omnibus) database through GSE176031 [101, 102]. Data analysis and visualization were performed on R software. A total of 8 cell types were defined manually by classic and well-established cellular markers as indicated in Chapter II (**Figure 28A**). The relative abundance of major cell types in each patient was plotted, and we noticed a higher abundance of T cells and myeloid cells in patients P5A, P5B, and P6A, while the other three patients (P7B, P7C, and P7D) had more epithelial cells compared to other cell types (**Figure 28B).** Next, the quantification of *FGFR1* and *CD8* expression was performed in the epithelial and T cell subtype, respectively. The result showed that P5B and P6A exhibited the lowest $FGFR1^+$ epithelial population, while P7B and P7C exhibited the highest $FGFR1^+$ epithelial cells (**Figure 28C**, left). On the contrary to

FGFR1 expressing cell population, the CD8α expression in patients P5B and P6A was significantly higher than in P7B and P7C (**Figure 28C**, right), suggesting less $CD8\alpha^+$ T cell infiltration in the TME of the patients with the highest tumor FGFR1 expression. To gain insight into the potential linkage between *FGFR1*$^+$ epithelial cells and $CD8\alpha^+$ T cells, a feature plot was generated to show the correlation between these two cell types specifically. The results showed lower *FGFR1*$^+$ epithelial cells together with more $CD8\alpha^+$ T cells in P5A, P5B, and P6A patients (**Figure 28D**). It is noteworthy that the dimensional reduction plot displaying the expression feature in different cell types showed no expression of *FGFR1* in T cells, which is consistent with the data mentioned earlier (Figure 16A). Taken all our data together, we found that an increased tumor *FGFR1*$^+$ epithelial cell population is negatively correlated to the $CD8\alpha^+$ T cell levels in PCa patient samples. This suggests that ectopic FGFR1 in PCa is a potential negative regulator for T cell infiltration into the TME. Also, the *FGFR1* is barely expressed in T cells, and thus the usage of an FGFR1 inhibitor may not disrupt T cell function due to the absence of the target. These data imply that blocking FGFR1 can serve as a potential strategy to retrieve immune responses in prostate tumors.

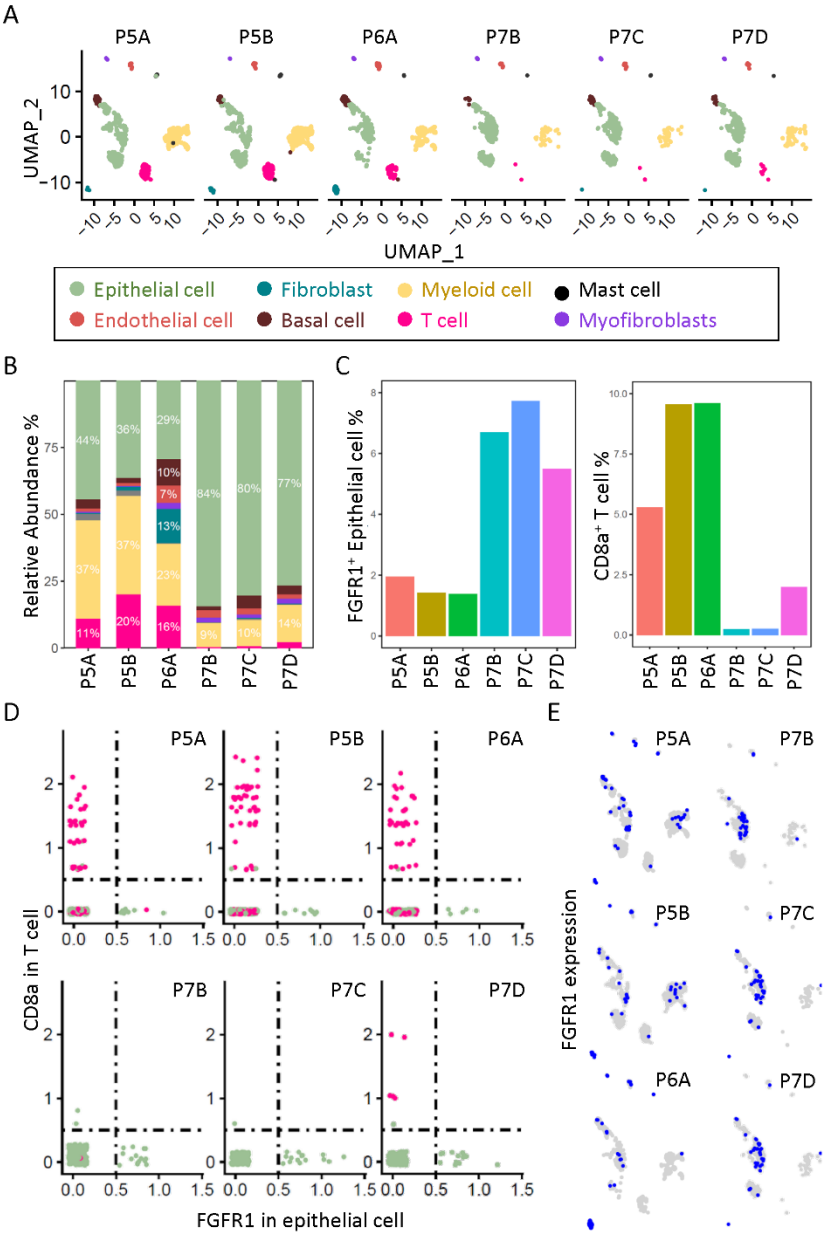

Figure 28 Correlation between epithelial FGFR1 expression and CD8$^+$ T cells.

A) UMAP plots of patient samples from GEO database (GSE176031), colored by identified cell types; B) Abundance of cell types from patient tissues; C) Percentage of FGFR1$^+$ epithelial cells and CD8α$^+$ T cells in total cells analyzed, respectively; D) Feature plot represents the correlation between FGFR1$^+$ epithelial cells (green) and CD8α$^+$ T cells (pink); E) Dimensional reduction plot displays the FGFR1$^+$ cells (blue).

CHAPTER IV

DISCUSSION AND FUTURE DIRECTIONS

Summary and discussion

PCa is the second leading cause of cancer death in males, with no cure available for the advanced stage so far [10]. The progression of PCa is a long multiple-step process that usually transforms tumors from slow-growing, androgen-sensitive to fast-growing, castration-resistant [2]. The high heterogeneity of primary PCa brings many challenges to the development of diagnostic methods and treatment strategies [133], which may also contribute to the low 5-year survival rate for advanced CRPC. Immunotherapy has gained huge success in treating multiple cancer types [134, 135] and generated rising expectations, yet Sipuleucel-T remains the only FDA-approved immunotherapy treatment for PCa [26, 27]. The effective usage of this vaccine is limited to a small population of PCa patients, tempering the enthusiasm for discovering new immune-based therapies by combining different drugs on the market. Immune checkpoints (such as PD-1) are acknowledged as one of the therapeutic hot spots, but the majority of the clinical trials of single-agent immunotherapy end up unsatisfactory [32-38], leaving CRPC as an "immune desert" to immunologists [31]. One of the possibilities that PCa has an "immune cold" TME is that it consists of immunosuppressive cells and molecules that make it difficult for immune cell infiltration, proliferation, and function, which leads to immunosuppression. Understanding the underlying mechanisms by which PCa cells remodel the TME will lead to the

development of novel strategies to convert the immune cold TME to the immune hot one and, therefore, improve the efficacy of immunotherapy for advanced CRPC.

Among various cellular signaling cascades that contribute PCa progression, ectopic FGFR1 signaling is a key player in PCa progression [4, 39, 46]. The ectopic expression of FGFR1 is conclusively demonstrated in human prostate carcinoma and contributes to the short survival time in CRPC [48-50]. Studies focusing on mouse Fgfr1 signaling reveal that ectopic Fgfr1 is sufficient for the initiation and progression of PCa [51-55]. However, the underlying mechanism of how FGFR1 promotes PCa progression is still elusive. Apart from the well-studied canonical downstream pathways, increasing evidence showed that FGFR1 also functions through non-canonical downstream targets, such as LDH, HK2, TAK1, and CHKA [57, 58, 76, 77]. A previous study showed that ectopic expression of FGFR1 increases the phosphorylation of LDHA and methylation of the LDHB promoter, leading to decreased lactate production [76]. Ablation of FGFR1 increased oxygen consumption in PCa cells, suggesting that FGFR1 promotes metabolic reprogramming from OXPHOS to aerobic glycolysis in PCa [76]. However, more convincing data are needed to reveal how ectopic FGFR1 is involved in the regulation of OXPHOS.

In this study, we reported that loss of FGFR1 signaling promoted mitochondrial respiration. We found that mitochondrial activity was increased upon FGFR1 ablation based on the following findings: 1) raised basal OCR and maximal respiration, representing the increased basal level and capacity of mitochondrial respiration; 2) increase of the ATP production associated with mitochondrial activity and steady

coupling efficiency, indicating more ATP production by a similar fraction of mitochondrial respiration, which suggests that the efficiency may increase; and 3) elevate the spare capacity. A similar phenotype was observed in DU145 cells with FGFR1 signaling blockade and was further confirmed by the blue light induced activation of optoR1 in DU145 cells. The (NADH/(NADH+FAD)) redox ratio, as an index representing the relative change from glucose catabolism to OXPHOS (NADH to NAD^+ and $FADH_2$ to FAD conversion occurs inside the ETC leading to a reduced (NADH/(NADH+FAD)) redox ratio when OXPHOS predominates [111]), was measured via fluorescence lifetime imaging. We found that the (NADH/(NADH+FAD)) redox ratio increased in $DU145^{\Delta R1}$ cells, suggesting that ablation of FGFR1 increased OXPHOS in DU145 cells. Also, upon FGFR1 ablation, both the short lifetime τ_1 and long lifetimes τ_2 of NAD(P)H decreased, suggesting that the free- and protein-bound forms of NADH were reduced in $DU145^{\Delta R1}$ cells. The significantly reduced the short lifetime component α_1 represents a lower utilization of free NAD(P)H upon FGFR1 ablation. This is the first report that ectopic FGFR1 negatively regulates mitochondrial function, which is supported by the increased oxygen consumption in $DU145^{\Delta R1}$ cells as reported previously [76].

On the contrary, aerobic glycolysis was significantly decreased in $DU145^{\Delta R1}$ cells with a dramatic decrease in basal and compensatory glycolysis, suggesting that cells may be more capable of adapting to mitochondrial dysfunction upon FGFR1 ablation. These data are consistent with previous reports: FGFR1 regulates LDH activities leading to the increased lactate accumulation in DU145 cells [76]. Knockdown

of FGFR1 expression reduced HK2 (hexokinase 2) expression in lymphatic endothelial cells, which also supports that loss of FGFR1 suppresses glycolysis in cells [136]. It is noteworthy that a short-term blockade of FGFR1 signaling leads to alteration in varying degrees for OXPHOS and glycolysis, compared to the effects of FGFR1 ablation. It might imply that FGFR1 regulation of these two metabolic pathways is not occurring at the same time but instead probably in chronological order. It could be due to different ways of regulation way (indirectly vs. directly, for example), but more efforts are needed to prove it.

Next, we quantified the ATP generated by mitochondrial respiration and glycolysis, respectively, and found that ablation of FGFR1 decreased glycoATP and increased mitoATP at the same time, suggesting that loss of FGFR1 reversed the metabolism changes in PCa cells by reducing glycolysis and increasing OXPHOS.

Apart from glucose-dependent pathways, fatty acid β-oxidation and glutaminolysis also fuel the TCA cycle and, therefore, contribute to OXPHOS [112, 113]. To identify which metabolic pathway(s) drive the increased OXPHOS in DU145$^{\Delta R1}$ cells, we measured the dependency and capacity of different metabolic pathways. Despite the possibility that FGFR1 is involved in the regulation of glutamine and fatty acid pathways, the major target for ectopic FGFR1 to suppress of OXPHOS in PCa cells is glycolysis. We then utilized RNA sequence to screen for candidate downstream targets of FGFR1 responsible for the metabolic alteration and identified two hits within the glucose-dependent pathways.

MPC1, as the first hit, is the transporter pumping pyruvate into mitochondria to serve as the major fuel of the TCA cycle, which is essential for pyruvate-driven mitochondrial respiration [137]. The increased expression level of MPC1 in aggressive PCa cell lines was reported previously, where DU145 cells (high FGFR1 expression) have significantly lower MPC1 expression compared to LNCaP cells (low FGFR1 expression level) [138], which supports our data that ablation of *FGFR1* leads to upregulation of *MPC1* in DU145 cells [138]. It also has been reported that decreased MPC1 is associated with a short survival time of PCa patients [138]. Suppression of MPC1 inhibits AR-driven PCa cell growth. However, AR negative DU145 cells did not respond to MPC1 inhibition by UK5099 [139]. The lack of response to MPC1 inhibition is potentially due to the low expression of MPC1 in DU145 cells. Our finding that *FGFR1* negatively regulates *MPC1* expression fills the gap of how MPC1 is regulated in AR negative cells.

PDP1, as the second hit, serves as the key regulator for the pyruvate dehydrogenase complex activity through ACAT1 and SIRT3 [140]. It is reported that PDP1 restores PDHA1 by dephosphorylation and subsequently regulates the activity of PDC [140, 141]. PDP1 expression is frequently increased in high-grade human prostate tumors [142]. Inhibition of FGFR1 decreases phosphorylation of PDP1 at Y381, which reduces the binding of PDP1 with ACAT1 but increases its binding with SIRT3 in H1299 cells [140]. The recruitment of ACAT1 promotes lysine acetylation of PDP1 and PDHA1 and, therefore, increases glycolysis [140]. These data support our finding that

ablation of *FGFR1* leads to increased expression of *PDP1* in DU145 cells, together with increased mitochondrial activity.

Taken together, ablation of FGFR1 in PCa cells promotes metabolic reprogramming from aerobic glycolysis to OXPHOS, which mainly occurs through the glucose-dependent pathway. MPC1 and PDP1 are potential downstream targets of FGFR1 to regulate this metabolic rewiring. More efforts are critically needed to fully understand the underlying mechanism.

One of the major consequences of metabolic reprogramming is tumor-derived lactate accumulation that decreases pH [143, 144], which promotes immune evasion by suppressing T cell-based immunity [73]. Lactate promotes FoxP3-mediated T cell polarization towards T_{reg} [75], as the pivotal mediator of immunosuppression [145]. A recent report found that lactate exhibits suppressive effects on T cell proliferation in a pH-independent manner, and it functions through lactate-induced reductive stress that accompanies the shift from NAD^+ to NADH [74]. These findings reveal that targeting tumor-derived lactate can potentially be a new strategy to warm up the immune cold TME in PCa. However, as aerobic glycolysis and OXPHOS are also needed for T cell activation and function, general metabolic inhibitors directly targeting these pathways will also disrupt T cell function as well, thus, can not be used to remodel the immune "cold" TME. We observed that FGFR1 ablation in PCa cells leads to decreased lactate production in our previous report [76]. In this report, we also found that ablation of FGFR1 decreased glycolysis. Since T cells do not express FGFR1, suppression of

FGFR1 can serve as a novel strategy to specifically reduce tumor-derived lactate and restore the TME to the immune permissive state.

We also found that ablation of FGFR1 in DU145 cells altered the cytokine profiles, evidenced by increased expression of cytokines that promotes T cell activation and proliferation, as well as decreasing expression of cytokines that suppress T cell activation. The results suggest that ablation of FGFR1 in PCa cells will promote T cell-based immunity through increased expression of anti-tumor cytokines and decreased immunosuppressive molecule secretion. To investigate how ectopic FGFR1 signaling promoted PCa cells to suppress T cell proliferation and function *in vitro*, Jurkat cells were treated with the medium conditioned by $DU145^{Ctrl}$ and $DU145^{\Delta R1}$ cells for five days, either with or without lactate acid addition. We found that the $DU145^{Ctrl}$ conditioned medium decreased Jurkat cell viability. However, the $DU145^{\Delta R1}$ conditioned medium did not elicit such activities. These data suggest that the absence of FGFR1 signaling blunts the activity of PCa cells to suppress Jurkat cell survival, likely through the secretion of metabolites and cytokines. To investigate how ectopic FGFR1 in PCa inhibits T cell-based immunity *in vivo*, we generated TRAMP mice bearing epithelial-specific ablation of *Fgfr1* ($TRAMP^{\Delta R1}$) as previously described [55]. As expected, the ablation significantly suppressed the tumor growth together with increased $CD3^{+}CD8^{+}$ T cells in the tumor. The results suggest that ablation of *Fgfr1* increases the tumor-infiltrating T cells and, therefore, increases the host anticancer immunity. However, the activity is limited and insufficient to diminish the tumors as reported previously.

As a hotspot of novel therapy development, antibodies targeting inhibitory checkpoint pathways that inhibit T cell-mediated immune response has been widely used to improve anti-cancer immunity. Since PCa has an unfavorable TME, the clinical development of monotherapy targeting PD-1 has been unsuccessful to date. Combination with other treatments has been proposed to improve anti-checkpoint therapy [132]. Therefore, we hypothesized that amelioration of the "immunologically cold" TME by suppressing ectopic FGFR1 signaling will enhance immune responses and improve the anti-checkpoint antibody therapies for PCa.

To further enhance the T cell-mediated anti-cancer immunity, we treated the mice with anti-PD-1 antibody that targets the checkpoint pathways, which inhibits T cell-mediated immune response. The anti-PD-1monoclonal antibody was administrated for two weeks in $TRAMP^{Ctrl}$ and $TRAMP^{\Delta R1}$ mice bearing similar sized tumors. We observed that tumor sizes shrank, together with increased $CD8^+$ tumor-infiltrating T cells in $TRAMP^{\Delta R1}$ mice treated with anti-PD-1 antibody. This suggests that ablation of *Fgfr1* improves the efficacy of anti-PD-1 antibody in Tramp mice. To further determine whether FGFR1 inhibition increases the efficacy of anti-checkpoint therapy, monoclonal antibody anti-PD-1 and AZD4547 (a small molecule specifically targeting FGFR1) were administrated either as a single agent(s) or in combination to TRAMP mice bearing similar sized tumors. A significantly increased $CD3^+CD8^+$ tumor-infiltrating T cells together with decreased tumor size was observed in the combination treatment group. The data indicate that a combination of AZD4547 and anti-PD-1 antibody effectively improves the $CD8^+$ T cell-mediated immune response and suppresses tumor growth in

the TRAMP model. It also reveals the potential of using an FGFR1 inhibitor as a novel combination strategy for PCa treatment.

To further investigate how ectopic FGFR1 expression affected T cell infiltration in human PCa, we downloaded and analyzed the scRNA-seq data from the public NCBI GEO database [101-103]. We found that compared with patients with high FGFR1 expressing PCa cells, patients with less FGFR expressing epithelial cells had more $CD8\alpha^+$ tumor-infiltrating T cells. The data suggest that increased FGFR1 expression epithelial cells population is a negative factor that limits $CD8\alpha^+$ T cell penetration in human PCa tissue. This is consistent with our data derive from the TRAMP model.

Our finding is the first report of testing the effect of FGFR1 specific inhibitor in combination with anti-PD-1 antibody in mouse PCa models. A recent report using Erdafitinib (an inhibitor of FGFR1-4) with anti-PD-1 for 6-weeks in FKNP mice demonstrated that such a combination suppressed tumor growth with increased cytotoxic and helper T cell infiltration in a non-small cell lung cancer model [146]. Similarly, combining PD173074 (an inhibitor of FGFR1 and FGFR3) with anti-PD-1 antibody also showed a synergistic antitumor effect with increased $CD4^+$ and $CD8^+$ T cells in the TME in a head and neck squamous cell carcinoma model [147]. Genetic knockout of FGFR1 downregulated PD-L1 and increased T cell infiltration in mice inoculated with pancreatic cancer cells [148]. Our findings extend the discovery that the combination FGFR1 inhibitor and anti-PD-1 antibody treatment increased T cell infiltration to PCa.

Taken together, our investigation identified FGFR1 as a potential target for selectively reducing the production and secretion of lactate and other

immunosuppressive molecules by cancer cells. We also determined that the combination of FGFR1 inhibitor and anti-PD-1 antibody strategy improved T cell infiltration likely via warming up the “immune cold” TME.

In summary, this study provides evidence that ectopic FGFR expression contributed to metabolic reprogramming in PCa, likely through non-canonical downstream signaling targets. It also provides a new strategy using FGFR1 inhibitor and anti-PD-1 antibody in combination for patients suffering from advanced CRPC.

Future directions

Although our data clearly demonstrate that ectopic FGFR1 signaling reprogramed cell metabolism and contributed to immune evasion, the detailed molecular mechanism and underlying downstream pathways still need to be unraveled. These hamper our insight into how inhibiting FGFR1 restores the immune response from the “immunologically cold” tumor microenvironment through metabolic reprogramming in PCa cells. The questions that need to be addressed are: in vivo characterization of how the loss of Fgfr1 changes metabolites and the altered metabolite profile affects tumor-infiltrating lymphocytes in PCa; in vivo characterization of the dose- and time-dependent effects of anti-PD-1 treatment to gain insight into the compound dynamics; validate the finding in other cell and mouse models to ensure our findings are not limited to specific experimental systems; cellular metabolites tracing glucose consumption should be added; finally, investigating the effect of PCa cells on the proliferation, differentiation, and function of human primary T cells.

Other than the underlying mechanism of how ectopic FGFR1 promotes OXPHOS and T cell infiltration in the TME, elucidating the temporal regulation of glycolysis and mitochondrial respiration pathways by FGFR1 would be an interesting future direction. Moreover, the decreased macrophage population following combination therapy, as indicated by our IMC data, may also serve as an attractive topic to discuss in the future.

REFERENCES

1. Siegel, R.L., et al., *Cancer statistics, 2022.* CA Cancer J Clin, 2022. **72**(1): p. 7-33.
2. McKeehan, W.L., et al., *Heparin-binding fibroblast growth factors and prostate cancer.* Adv Exp Med Biol, 1993. **330**: p. 203-13.
3. Tyekucheva, S., et al., *Stromal and epithelial transcriptional map of initiation progression and metastatic potential of human prostate cancer.* Nat Commun, 2017. **8**(1): p. 420.
4. Wang, C., et al., *Intrinsic FGFR2 and Ectopic FGFR1 Signaling in the Prostate and Prostate Cancer.* Front Genet, 2019. **10**: p. 12.
5. Shen, M.M. and C. Abate-Shen, *Molecular genetics of prostate cancer: new prospects for old challenges.* Genes Dev, 2010. **24**(18): p. 1967-2000.
6. Wang, Y., et al., *Molecular events in neuroendocrine prostate cancer development.* Nat Rev Urol, 2021. **18**(10): p. 581-596.
7. Arora, K. and C.E. Barbieri, *Molecular Subtypes of Prostate Cancer.* Curr Oncol Rep, 2018. **20**(8): p. 58.
8. Zynger, D.L. and X. Yang, *High-grade prostatic intraepithelial neoplasia of the prostate: the precursor lesion of prostate cancer.* Int J Clin Exp Pathol, 2009. **2**(4): p. 327-38.
9. Knudsen, B.S. and V. Vasioukhin, *Mechanisms of prostate cancer initiation and progression.* Adv Cancer Res, 2010. **109**: p. 1-50.

10. Tarver, T., *CANCER FACTS & FIGURES 2012. American Cancer Society (ACS).* Journal of Consumer Health on the Internet, 2012. **16**(3): p. 366-367.

11. Catalona, W.J., *Prostate Cancer Screening.* Med Clin North Am, 2018. **102**(2): p. 199-214.

12. Hu, J.C., et al., *Increase in Prostate Cancer Distant Metastases at Diagnosis in the United States.* JAMA Oncol, 2017. **3**(5): p. 705-707.

13. Sun, Y., et al., *Multiparametric MRI and radiomics in prostate cancer: a review.* Australas Phys Eng Sci Med, 2019. **42**(1): p. 3-25.

14. Haffner, M.C., et al., *Genomic and phenotypic heterogeneity in prostate cancer.* Nat Rev Urol, 2021. **18**(2): p. 79-92.

15. Sebesta, E.M. and C.B. Anderson, *The Surgical Management of Prostate Cancer.* Semin Oncol, 2017. **44**(5): p. 347-357.

16. Kamran, S.C. and A.V. D'Amico, *Radiation Therapy for Prostate Cancer.* Hematol Oncol Clin North Am, 2020. **34**(1): p. 45-69.

17. Parker, C., et al., *Prostate cancer: ESMO Clinical Practice Guidelines for diagnosis, treatment and follow-up.* Ann Oncol, 2020. **31**(9): p. 1119-1134.

18. Evans, A.J., *Treatment effects in prostate cancer.* Mod Pathol, 2018. **31**(S1): p. S110-121.

19. Arsov, C., et al., *Current second-line treatment options for patients with castration resistant prostate cancer (CRPC) resistant to docetaxel.* Urol Oncol, 2012. **30**(6): p. 762-71.

20. Mostaghel, E.A., *Abiraterone in the treatment of metastatic castration-resistant prostate cancer.* Cancer Manag Res, 2014. **6**: p. 39-51.

21. Borno, H.T. and E.J. Small, *Apalutamide and its use in the treatment of prostate cancer.* Future Oncol, 2019. **15**(6): p. 591-599.

22. Villanueva, C., et al., *Cabazitaxel: a novel microtubule inhibitor.* Drugs, 2011. **71**(10): p. 1251-8.

23. Abbasi, A., et al., *Darolutamide as a Second-Generation Androgen Receptor Inhibitor in the Treatment of Prostate Cancer.* Curr Mol Med, 2021. **21**(4): p. 332-346.

24. Verweij, J., M. Clavel, and B. Chevalier, *Paclitaxel (Taxol) and docetaxel (Taxotere): not simply two of a kind.* Ann Oncol, 1994. **5**(6): p. 495-505.

25. Wang, Y., et al., *Mechanisms of enzalutamide resistance in castration-resistant prostate cancer and therapeutic strategies to overcome it.* Br J Pharmacol, 2021. **178**(2): p. 239-261.

26. Graff, J.N. and E.D. Chamberlain, *Sipuleucel-T in the treatment of prostate cancer: an evidence-based review of its place in therapy.* Core Evid, 2015. **10**: p. 1-10.

27. Kantoff, P.W., et al., *Sipuleucel-T immunotherapy for castration-resistant prostate cancer.* N Engl J Med, 2010. **363**(5): p. 411-22.

28. Rizzo, A., et al., *Is There a Role for Immunotherapy in Prostate Cancer?* Cells, 2020. **9**(9).

29. Caram, M.E.V., et al., *Factors Associated With Use of Sipuleucel-T to Treat Patients With Advanced Prostate Cancer.* JAMA Netw Open, 2019. **2**(4): p. e192589.

30. Slovin, S.F., *Immunotherapy for castration-resistant prostate cancer: has its time arrived?* Expert Opin Biol Ther, 2020. **20**(5): p. 481-487.

31. Cha, H.R., J.H. Lee, and S. Ponnazhagan, *Revisiting Immunotherapy: A Focus on Prostate Cancer.* Cancer Res, 2020. **80**(8): p. 1615-1623.

32. Kwon, E.D., et al., *Ipilimumab versus placebo after radiotherapy in patients with metastatic castration-resistant prostate cancer that had progressed after docetaxel chemotherapy (CA184-043): a multicentre, randomised, double-blind, phase 3 trial.* Lancet Oncol, 2014. **15**(7): p. 700-12.

33. Beer, T.M., et al., *Randomized, Double-Blind, Phase III Trial of Ipilimumab Versus Placebo in Asymptomatic or Minimally Symptomatic Patients With Metastatic Chemotherapy-Naive Castration-Resistant Prostate Cancer.* J Clin Oncol, 2017. **35**(1): p. 40-47.

34. Hansen, A.R., et al., *Pembrolizumab for advanced prostate adenocarcinoma: findings of the KEYNOTE-028 study.* Ann Oncol, 2018. **29**(8): p. 1807-1813.

35. Antonarakis, E.S., et al., *Pembrolizumab for Treatment-Refractory Metastatic Castration-Resistant Prostate Cancer: Multicohort, Open-Label Phase II KEYNOTE-199 Study.* J Clin Oncol, 2020. **38**(5): p. 395-405.

36. Petrylak, D.P., et al., *Safety and Clinical Activity of Atezolizumab in Patients with Metastatic Castration-Resistant Prostate Cancer: A Phase I Study.* Clin Cancer Res, 2021. **27**(12): p. 3360-3369.

37. Pal, S.K., et al., *Cabozantinib in Combination With Atezolizumab for Advanced Renal Cell Carcinoma: Results From the COSMIC-021 Study.* J Clin Oncol, 2021. **39**(33): p. 3725-3736.

38. Wong, Y.N.S., et al., *Nivolumab and ipilimumab treatment in prostate cancer with an immunogenic signature (NEPTUNES).* Journal of Clinical Oncology, 2019. **37**(15_suppl): p. TPS5090-TPS5090.

39. Corn, P.G., et al., *Targeting fibroblast growth factor pathways in prostate cancer.* Clin Cancer Res, 2013. **19**(21): p. 5856-66.

40. Opalinski, L., et al., *The autoinhibitory function of D1 domain of FGFR1 goes beyond the inhibition of ligand binding.* Int J Biochem Cell Biol, 2017. **89**: p. 193-198.

41. Kalinina, J., et al., *The alternatively spliced acid box region plays a key role in FGF receptor autoinhibition.* Structure, 2012. **20**(1): p. 77-88.

42. Wang, F., et al., *Alternately spliced NH2-terminal immunoglobulin-like Loop I in the ectodomain of the fibroblast growth factor (FGF) receptor 1 lowers affinity for both heparin and FGF-1.* J Biol Chem, 1995. **270**(17): p. 10231-5.

43. Goetz, R. and M. Mohammadi, *Exploring mechanisms of FGF signalling through the lens of structural biology.* Nat Rev Mol Cell Biol, 2013. **14**(3): p. 166-80.

44. Yeh, B.K., et al., *Structural basis by which alternative splicing confers specificity in fibroblast growth factor receptors.* Proc Natl Acad Sci U S A, 2003. **100**(5): p. 2266-71.

45. Miki, T., et al., *Determination of ligand-binding specificity by alternative splicing: two distinct growth factor receptors encoded by a single gene.* Proc Natl Acad Sci U S A, 1992. **89**(1): p. 246-50.

46. Lin, Y. and F. Wang, *FGF signalling in prostate development, tissue homoeostasis and tumorigenesis.* Biosci Rep, 2010. **30**(5): p. 285-91.

47. Chae, Y.K., et al., *Inhibition of the fibroblast growth factor receptor (FGFR) pathway: the current landscape and barriers to clinical application.* Oncotarget, 2017. **8**(9): p. 16052-16074.

48. Armstrong, K., et al., *Upregulated FGFR1 expression is associated with the transition of hormone-naive to castrate-resistant prostate cancer.* Br J Cancer, 2011. **105**(9): p. 1362-9.

49. Li, X., et al., *Fibroblast growth factors, old kids on the new block.* Semin Cell Dev Biol, 2016. **53**: p. 155-67.

50. Taylor, B.S., et al., *Integrative genomic profiling of human prostate cancer.* Cancer Cell, 2010. **18**(1): p. 11-22.

51. Jin, C., et al., *Cooperation between ectopic FGFR1 and depression of FGFR2 in induction of prostatic intraepithelial neoplasia in the mouse prostate.* Cancer Res, 2003. **63**(24): p. 8784-90.

52. Wang, F., et al., *Chronic activity of ectopic type 1 fibroblast growth factor receptor tyrosine kinase in prostate epithelium results in hyperplasia accompanied by intraepithelial neoplasia.* Prostate, 2004. **58**(1): p. 1-12.

53. Acevedo, V.D., et al., *Inducible FGFR-1 activation leads to irreversible prostate adenocarcinoma and an epithelial-to-mesenchymal transition.* Cancer Cell, 2007. **12**(6): p. 559-71.

54. Freeman, K.W., et al., *Inducible prostate intraepithelial neoplasia with reversible hyperplasia in conditional FGFR1-expressing mice.* Cancer Res, 2003. **63**(23): p. 8256-63.

55. Yang, F., et al., *FGFR1 is essential for prostate cancer progression and metastasis.* Cancer Res, 2013. **73**(12): p. 3716-24.

56. Gallo, L.H., et al., *Functions of Fibroblast Growth Factor Receptors in cancer defined by novel translocations and mutations.* Cytokine Growth Factor Rev, 2015. **26**(4): p. 425-49.

57. Wang, C., et al., *Ectopic fibroblast growth factor receptor 1 promotes inflammation by promoting nuclear factor-kappaB signaling in prostate cancer cells.* J Biol Chem, 2018. **293**(38): p. 14839-14849.

58. Fan, Z., et al., *Crosstalk of FGFR1 signaling and choline metabolism promotes cell proliferation and survival in prostate cancer cells.* Int J Cancer, 2022.

59. Hanahan, D. and R.A. Weinberg, *Hallmarks of cancer: the next generation.* Cell, 2011. **144**(5): p. 646-74.

60. Liberti, M.V. and J.W. Locasale, *The Warburg Effect: How Does it Benefit Cancer Cells?* Trends Biochem Sci, 2016. **41**(3): p. 211-218.

61. Lu, J., M. Tan, and Q. Cai, *The Warburg effect in tumor progression: mitochondrial oxidative metabolism as an anti-metastasis mechanism.* Cancer Lett, 2015. **356**(2 Pt A): p. 156-64.

62. Tang, J.X., et al., *Mitochondrial OXPHOS Biogenesis: Co-Regulation of Protein Synthesis, Import, and Assembly Pathways.* Int J Mol Sci, 2020. **21**(11).

63. Warburg, O., *On the metabolism of cancer cells.* Naturwissenschaften, 1924. **12**: p. 1131-1137.

64. Warburg, O., F. Wind, and E. Negelein, *The Metabolism of Tumors in the Body.* J Gen Physiol, 1927. **8**(6): p. 519-30.

65. Sciacovelli, M., et al., *The metabolic alterations of cancer cells.* Methods Enzymol, 2014. **542**: p. 1-23.

66. Sahin, E., et al., *Clinical significance of incidental FDG uptake in the prostate gland detected by PET/CT.* Int J Clin Exp Med, 2015. **8**(7): p. 10577-85.

67. Albers, M.J., et al., *Hyperpolarized 13C lactate, pyruvate, and alanine: noninvasive biomarkers for prostate cancer detection and grading.* Cancer Res, 2008. **68**(20): p. 8607-15.

68. Granlund, K.L., et al., *Hyperpolarized MRI of Human Prostate Cancer Reveals Increased Lactate with Tumor Grade Driven by Monocarboxylate Transporter 1.* Cell Metab, 2020. **31**(1): p. 105-114 e3.

69. Schopf, B., et al., *OXPHOS remodeling in high-grade prostate cancer involves mtDNA mutations and increased succinate oxidation.* Nat Commun, 2020. **11**(1): p. 1487.

70. Vander Heiden, M.G., L.C. Cantley, and C.B. Thompson, *Understanding the Warburg effect: the metabolic requirements of cell proliferation.* Science, 2009. **324**(5930): p. 1029-33.

71. Fan, C., et al., *Emerging role of metabolic reprogramming in tumor immune evasion and immunotherapy.* Sci China Life Sci, 2021. **64**(4): p. 534-547.

72. Ngwa, V.M., et al., *Microenvironmental Metabolism Regulates Antitumor Immunity.* Cancer Res, 2019. **79**(16): p. 4003-4008.

73. Hayes, C., et al., *The oncogenic and clinical implications of lactate induced immunosuppression in the tumour microenvironment.* Cancer Lett, 2021. **500**: p. 75-86.

74. Quinn, W.J., 3rd, et al., *Lactate Limits T Cell Proliferation via the NAD(H) Redox State.* Cell Rep, 2020. **33**(11): p. 108500.

75. Comito, G., et al., *Lactate modulates CD4(+) T-cell polarization and induces an immunosuppressive environment, which sustains prostate carcinoma progression via TLR8/miR21 axis.* Oncogene, 2019. **38**(19): p. 3681-3695.

76. Liu, J., et al., *Aberrant FGFR Tyrosine Kinase Signaling Enhances the Warburg Effect by Reprogramming LDH Isoform Expression and Activity in Prostate Cancer.* Cancer Res, 2018. **78**(16): p. 4459-4470.

77. Yu, P., et al., *FGF-dependent metabolic control of vascular development.* Nature, 2017. **545**(7653): p. 224-228.

78. Sanjana, N.E., O. Shalem, and F. Zhang, *Improved vectors and genome-wide libraries for CRISPR screening.* Nat Methods, 2014. **11**(8): p. 783-784.

79. Shalem, O., et al., *Genome-scale CRISPR-Cas9 knockout screening in human cells.* Science, 2014. **343**(6166): p. 84-87.

80. Kim, N., et al., *Spatiotemporal control of fibroblast growth factor receptor signals by blue light.* Chem Biol, 2014. **21**(7): p. 903-12.

81. Wingett, S.W. and S. Andrews, *FastQ Screen: A tool for multi-genome mapping and quality control.* F1000Res, 2018. **7**: p. 1338.

82. Ewels, P., et al., *MultiQC: summarize analysis results for multiple tools and samples in a single report.* Bioinformatics, 2016. **32**(19): p. 3047-8.

83. Trapnell, C., et al., *Differential gene and transcript expression analysis of RNA-seq experiments with TopHat and Cufflinks.* Nat Protoc, 2012. **7**(3): p. 562-78.

84. Trapnell, C., et al., *Transcript assembly and quantification by RNA-Seq reveals unannotated transcripts and isoform switching during cell differentiation.* Nat Biotechnol, 2010. **28**(5): p. 511-5.

85. Roberts, A., et al., *Improving RNA-Seq expression estimates by correcting for fragment bias.* Genome Biol, 2011. **12**(3): p. R22.

86. Roberts, A., et al., *Identification of novel transcripts in annotated genomes using RNA-Seq.* Bioinformatics, 2011. **27**(17): p. 2325-9.

87. Trapnell, C., et al., *Differential analysis of gene regulation at transcript resolution with RNA-seq.* Nat Biotechnol, 2013. **31**(1): p. 46-53.

88. Walsh, A.J., et al., *Classification of T-cell activation via autofluorescence lifetime imaging.* Nat Biomed Eng, 2021. **5**(1): p. 77-88.

89. Theodossiou, A., et al., *Autofluorescence Imaging to Evaluate Cellular Metabolism.* J Vis Exp, 2021(177).

90. Walsh, A.J., et al., *Optical metabolic imaging identifies glycolytic levels, subtypes, and early-treatment response in breast cancer.* Cancer Res, 2013. **73**(20): p. 6164-74.

91. Lin, Y., et al., *Fibroblast growth factor receptor 2 tyrosine kinase is required for prostatic morphogenesis and the acquisition of strict androgen dependency for adult tissue homeostasis.* Development, 2007. **134**(4): p. 723-34.

92. Zhang, Y., et al., *Role of epithelial cell fibroblast growth factor receptor substrate 2alpha in prostate development, regeneration and tumorigenesis.* Development, 2008. **135**(4): p. 775-84.

93. Wang, C., et al., *Type 1 fibroblast growth factor receptor in cranial neural crest cell-derived mesenchyme is required for palatogenesis.* J Biol Chem, 2013. **288**(30): p. 22174-83.

94. Wirtzfeld, L.A., et al., *A new three-dimensional ultrasound microimaging technology for preclinical studies using a transgenic prostate cancer mouse model.* Cancer Res, 2005. **65**(14): p. 6337-45.

95. Ni, J., et al., *Monitoring Prostate Tumor Growth in an Orthotopic Mouse Model Using Three-Dimensional Ultrasound Imaging Technique.* Transl Oncol, 2016. **9**(1): p. 41-45.

96. Faustino-Rocha, A., et al., *Estimation of rat mammary tumor volume using caliper and ultrasonography measurements.* Lab Anim (NY), 2013. **42**(6): p. 217-24.

97. Livak, K.J. and T.D. Schmittgen, *Analysis of relative gene expression data using real-time quantitative PCR and the 2(-Delta Delta C(T)) Method.* Methods, 2001. **25**(4): p. 402-8.

98. Vito RT Zanotelli, B.B., *ImcSegmentationPipeline: A pixelclassification based multiplexed image segmentation pipeline.* 2017.

99. Schapiro, D., et al., *histoCAT: analysis of cell phenotypes and interactions in multiplex image cytometry data.* Nat Methods, 2017. **14**(9): p. 873-876.

100. Henry, G.H., et al., *A Cellular Anatomy of the Normal Adult Human Prostate and Prostatic Urethra.* Cell Rep, 2018. **25**(12): p. 3530-3542 e5.

101. Edgar, R., M. Domrachev, and A.E. Lash, *Gene Expression Omnibus: NCBI gene expression and hybridization array data repository.* Nucleic Acids Res, 2002. **30**(1): p. 207-10.

102. Barrett, T., et al., *NCBI GEO: archive for functional genomics data sets--update.* Nucleic Acids Res, 2013. **41**(Database issue): p. D991-5.

103. Song, H., et al., *Single-cell analysis of human primary prostate cancer reveals the heterogeneity of tumor-associated epithelial cell states.* Nat Commun, 2022. **13**(1): p. 141.

104. Hao, Y., et al., *Integrated analysis of multimodal single-cell data.* Cell, 2021. **184**(13): p. 3573-3587 e29.

105. McInnes, L., J. Healy, and J. Melville *UMAP: Uniform Manifold Approximation and Projection for Dimension Reduction*. 2018. arXiv:1802.03426.

106. Labanca, E., et al., *Fibroblast Growth Factor Receptor 1 Drives the Metastatic Progression of Prostate Cancer.* Eur Urol Oncol, 2021.

107. Tucker, J.A., et al., *Structural insights into FGFR kinase isoform selectivity: diverse binding modes of AZD4547 and ponatinib in complex with FGFR1 and FGFR4.* Structure, 2014. **22**(12): p. 1764-1774.

108. Mohammadi, M., J. Schlessinger, and S.R. Hubbard, *Structure of the FGF receptor tyrosine kinase domain reveals a novel autoinhibitory mechanism.* Cell, 1996. **86**(4): p. 577-87.

109. Lew, E.D., et al., *The precise sequence of FGF receptor autophosphorylation is kinetically driven and is disrupted by oncogenic mutations.* Sci Signal, 2009. **2**(58): p. ra6.

110. Hu, L., et al., *Fluorescence intensity and lifetime redox ratios detect metabolic perturbations in T cells.* Biomed Opt Express, 2020. **11**(10): p. 5674-5688.

111. Alhallak, K., et al., *Optical redox ratio identifies metastatic potential-dependent changes in breast cancer cell metabolism.* Biomed Opt Express, 2016. **7**(11): p. 4364-4374.

112. Maher, M., et al., *Epigenetic-Transcriptional Regulation of Fatty Acid Metabolism and Its Alterations in Leukaemia.* Front Genet, 2018. **9**: p. 405.

113. Jin, L., G.N. Alesi, and S. Kang, *Glutaminolysis as a target for cancer therapy.* Oncogene, 2016. **35**(28): p. 3619-25.

114. Yamashita, Y., et al., *A Chemical Proteomic Probe for the Mitochondrial Pyruvate Carrier Complex.* Angew Chem Int Ed Engl, 2020. **59**(10): p. 3896-3899.

115. Song, M., et al., *Recent Development of Small Molecule Glutaminase Inhibitors.* Curr Top Med Chem, 2018. **18**(6): p. 432-443.

116. O'Connor, R.S., et al., *The CPT1a inhibitor, etomoxir induces severe oxidative stress at commonly used concentrations.* Sci Rep, 2018. **8**(1): p. 6289.

117. McCommis, K.S. and B.N. Finck, *Mitochondrial pyruvate transport: a historical perspective and future research directions.* Biochem J, 2015. **466**(3): p. 443-54.

118. De Meirleir, L., *Disorders of pyruvate metabolism.* Handb Clin Neurol, 2013. **113**: p. 1667-73.

119. Peters, S.J., *Regulation of PDH activity and isoform expression: diet and exercise.* Biochem Soc Trans, 2003. **31**(Pt 6): p. 1274-80.

120. Choi, S.Y., et al., *Cancer-generated lactic acid: a regulatory, immunosuppressive metabolite?* J Pathol, 2013. **230**(4): p. 350-5.

121. Brand, A., et al., *LDHA-Associated Lactic Acid Production Blunts Tumor Immunosurveillance by T and NK Cells.* Cell Metab, 2016. **24**(5): p. 657-671.

122. Eleftheriadis, T., et al., *In human alloreactive CD4(+) T-cells, dichloroacetate inhibits aerobic glycolysis, induces apoptosis and favors differentiation towards the regulatory T-cell subset instead of effector T-cell subsets.* Mol Med Rep, 2016. **13**(4): p. 3370-6.

123. Cao, Y., J.C. Rathmell, and A.N. Macintyre, *Metabolic reprogramming towards aerobic glycolysis correlates with greater proliferative ability and resistance to metabolic inhibition in CD8 versus CD4 T cells.* PLoS One, 2014. **9**(8): p. e104104.

124. Wanhainen, K.M., S.C. Jameson, and H.B. da Silva, *Self-Regulation of Memory CD8 T Cell Metabolism through Extracellular ATP Signaling.* Immunometabolism, 2019. **1**(1).

125. Zhang, Y., Y. Liu, and Y. Xu, *Interleukin-24 Regulates T Cell Activity in Patients With Colorectal Adenocarcinoma.* Front Oncol, 2019. **9**: p. 1401.

126. Curti, A., et al., *Interleukin-11 induces Th2 polarization of human CD4(+) T cells.* Blood, 2001. **97**(9): p. 2758-63.

127. Holscher, C., *The power of combinatorial immunology: IL-12 and IL-12-related dimeric cytokines in infectious diseases.* Med Microbiol Immunol, 2004. **193**(1): p. 1-17.

128. Kaplanski, G., *Interleukin-18: Biological properties and role in disease pathogenesis.* Immunol Rev, 2018. **281**(1): p. 138-153.

129. Yang, S., W. Wei, and Q. Zhao, *B7-H3, a checkpoint molecule, as a target for cancer immunotherapy.* Int J Biol Sci, 2020. **16**(11): p. 1767-1773.

130. Marin-Acevedo, J.A., et al., *Next generation of immune checkpoint therapy in cancer: new developments and challenges.* J Hematol Oncol, 2018. **11**(1): p. 39.

131. Goswami, S., A. Aparicio, and S.K. Subudhi, *Immune Checkpoint Therapies in Prostate Cancer.* Cancer J, 2016. **22**(2): p. 117-20.

132. Lu, X., et al., *Effective combinatorial immunotherapy for castration-resistant prostate cancer.* Nature, 2017. **543**(7647): p. 728-732.

133. Tang, D.G., *Understanding and targeting prostate cancer cell heterogeneity and plasticity.* Semin Cancer Biol, 2021.

134. Kruger, S., et al., *Advances in cancer immunotherapy 2019 - latest trends.* J Exp Clin Cancer Res, 2019. **38**(1): p. 268.

135. Gong, J., et al., *Development of PD-1 and PD-L1 inhibitors as a form of cancer immunotherapy: a comprehensive review of registration trials and future considerations.* J Immunother Cancer, 2018. **6**(1): p. 8.

136. Song, H., et al., *Metabolic flexibility maintains proliferation and migration of FGFR signaling-deficient lymphatic endothelial cells.* J Biol Chem, 2021. **297**(4): p. 101149.

137. Negreiros, R.S., et al., *Mitochondrial Pyruvate Carrier Subunits Are Essential for Pyruvate-Driven Respiration, Infectivity, and Intracellular Replication of Trypanosoma cruzi.* mBio, 2021. **12**(2).

138. Li, X., et al., *MPC1 and MPC2 expressions are associated with favorable clinical outcomes in prostate cancer.* BMC Cancer, 2016. **16**(1): p. 894.

139. Bader, D.A., et al., *Mitochondrial pyruvate import is a metabolic vulnerability in androgen receptor-driven prostate cancer.* Nat Metab, 2019. **1**(1): p. 70-85.

140. Fan, J., et al., *Tyr phosphorylation of PDP1 toggles recruitment between ACAT1 and SIRT3 to regulate the pyruvate dehydrogenase complex.* Mol Cell, 2014. **53**(4): p. 534-48.

141. Patel, M.S., et al., *The pyruvate dehydrogenase complexes: structure-based function and regulation.* J Biol Chem, 2014. **289**(24): p. 16615-23.

142. Chen, J., et al., *Compartmentalized activities of the pyruvate dehydrogenase complex sustain lipogenesis in prostate cancer.* Nat Genet, 2018. **50**(2): p. 219-228.

143. Dumas, J.F., et al., *Metabolic reprogramming in cancer cells, consequences on pH and tumour progression: Integrated therapeutic perspectives with dietary lipids as adjuvant to anticancer treatment.* Semin Cancer Biol, 2017. **43**: p. 90-110.

144. Chen, A.N., et al., *Lactylation, a Novel Metabolic Reprogramming Code: Current Status and Prospects.* Front Immunol, 2021. **12**: p. 688910.

145. Facciabene, A., G.T. Motz, and G. Coukos, *T-regulatory cells: key players in tumor immune escape and angiogenesis.* Cancer Res, 2012. **72**(9): p. 2162-71.

146. Palakurthi, S., et al., *The Combined Effect of FGFR Inhibition and PD-1 Blockade Promotes Tumor-Intrinsic Induction of Antitumor Immunity.* Cancer Immunol Res, 2019. **7**(9): p. 1457-1471.

147. Kono, M., et al., *Immunomodulation via FGFR inhibition augments FGFR1 targeting T-cell based antitumor immunotherapy for head and neck squamous cell carcinoma.* Oncoimmunology, 2022. **11**(1): p. 2021619.

148. Glorieux, C., et al., *Regulation of PD-L1 expression in K-ras-driven cancers through ROS-mediated FGFR1 signaling.* Redox Biol, 2021. **38**: p. 101780.